Continental Shelf Research 93 (2015) 39–57

Contents lists available at ScienceDirect

Continental Shelf Research

journal homepage: www.elsevier.com/locate/csr

Intra- and inter-tidal variability of the vertical current structure in the Marsdiep basin

J.J. de Vries*, H. Ridderinkhof, L.R.M. Maas, H.M. van Aken

NIOZ Royal Netherlands Institute for Sea Research, NL-1790 AB Den Burg, The Netherlands

ARTICLE INFO

Article history:
Received 9 April 2014
Received in revised form
18 November 2014
Accepted 5 December 2014
Available online 12 December 2014

Keywords:
Vertical current structure
Western Dutch Wadden Sea
Mid-depth velocity maximum
Cross-stream tidal straining
Asymmetry in bed friction
Complex bathymetry

ABSTRACT

The vertical structure of the along-stream current in the main channel of the periodically-stratified estuarine Marsdiep basin is investigated by combining velocity measurements collected during three different seasons with a one-dimensional water column model. The observed vertical shears in the lowest part of the water column are greater during ebb than during flood due to an asymmetry in drag coefficient (i.e. bed friction), which is most likely determined by the surrounding complex bathymetry. This asymmetry is usually not incorporated in models. Furthermore, a mid-depth velocity maximum is observed and simulated during early and late flood which is generated by along-stream and cross-stream tidal straining, respectively. Negative shears are present in the upper part of the water column during flood, which correlate well with the along-stream salinity gradient. The mid-depth velocity maximum during late flood results in an early current reversal in the upper part of the water column. The elevated vertical shears during ebb are able to reduce vertical stratification induced by along-stream tidal straining, whereas cross-stream tidal straining during late flood promotes the generation of vertical stratification. The simulations suggest that these processes are most important during spring tide conditions. This study has demonstrated that an asymmetry in bed friction and the presence of density gradients both have a strong impact on the vertical structure of along-stream velocity in the Marsdiep basin.

1. Introduction

Currents in estuaries and coastal seas are the main transport agents of suspended matter. The net transport patterns of plankton, larvae, nutrients, pollutants and suspended sediment are partly determined by the residual current. The vertical distribution of suspended matter varies in the water column and therefore for understanding the vertical and horizontal exchange patterns in an estuary, it is important to also take the vertical profile of the current and salinity into account.

In estuaries, the shape of the vertical profile of along-stream velocity is determined by the interaction of the barotropic and baroclinic pressure gradients, which creates a difference in the shape of the vertical profiles between ebb and flood (Simpson et al., 1990; Jay and Musiak, 1996; Seim et al., 2002; MacCready and Geyer, 2010; Geyer and MacCready, 2013 and references therein). During flood, the direction of the baroclinic force in the near-bottom layer coincides with the direction of the barotropic force, which in the absence of bed friction and vertical mixing would result in the strongest velocities near the seabed (Valle-levinson and Wilson, 1994). However, the seabed imposes a frictional drag on the tidal currents, which, in combination with the strong near-bed velocities during flood, results in greater near-bed shears, potentially generating a well-mixed water column (e.g. Jay and Musiak, 1996). During ebb, the baroclinic and barotropic forces oppose each other near the bottom, generating smaller shears at the bottom and greater shears in the upper part of the water column. Furthermore, fresher water higher up in the water column is advected over saltier water during ebb which generates vertical stratification, a process called tidal straining (van Aken, 1986; Simpson et al., 1990). Classical tidal straining only generates vertical stratification during ebb, because advection of salty water over less salty water during flood results in unstable stratification, which generates vertical mixing.

The steady baroclinic pressure gradient (Pritchard, 1956; Hansen and Rattray, 1966) and the strain-induced periodic stratification (Simpson et al., 1990; Jay and Musiak, 1996) modify the shape of the vertical profile in estuaries. Burchard and Hetland (2010) demonstrated with model simulations that tidal straining contributed approximately two-thirds to the residual circulation, whereas the baroclinic tide itself contributed only one-third in periodically-stratified estuaries. Both mechanisms are able to

* Corresponding author. Fax: +31 222319674.
E-mail address: jurre.de.vries@nioz.nl (J.J. de Vries).

http://dx.doi.org/10.1016/j.csr.2014.12.002
0278-4343/

modify the shape of the vertical profile of along-stream velocity and thereby determine the vertical profile of residual circulation.

Commonly, the difference in shape of the vertical profiles between ebb and flood results in the classical residual estuarine circulation with inflow at the bottom and outflow at the surface (e.g. Geyer et al., 2000; Stacey et al., 2001, 2008; Seim et al., 2002; Murphy and Valle-Levinson, 2008). There also exist inverse estuaries, where the baroclinic force near the bottom is directed in the opposite direction (towards the sea), e.g. by strong evaporation within the estuary, which has an inverse effect on the vertical profile of ebb and flood and produces an inverse estuarine circulation cell with the near-bed and near-surface residual currents directed down- and up-estuary, respectively (e.g. Winant and Gutierrez de Velosco, 2003).

Additionally, the shape of the vertical profiles is strongly influenced by the impact of bed friction on the current. Generally, the drag coefficient is taken as a measure for bed friction and is in the order of $1-3\times10^{-3}$ (e.g. Geyer et al., 2000; Seim et al., 2002; Li et al., 2004). However, greater values have also been observed up to 1×10^{-2} (Cudaback and Jay, 2001; Fong et al., 2009). In addition, the drag coefficient has been observed to vary from neap to spring tide, and from ebb to flood (Geyer et al., 2000; Li et al., 2004; Fong et al., 2009). The drag imposed on the currents by the seabed is only transferred up in the water column to a certain height, called the bottom boundary layer. Stacey and Ralston (2005) demonstrated that the bottom boundary layer does not cover the entire water column during the entire tidal cycle in the northern San Francisco Bay, which was also found in the Marsdiep basin (De Vries et al., 2014). Also, several studies have shown that form drag is another important mechanism which is able to dissipate tidal energy (Chriss and Caldwell, 1982; Moum and Nash, 2000; Warner et al., 2013). Form drag is the drag imposed on the fluid by pressure differences generated by currents traversing non-uniform bathymetry, which may be up to 10–50 times greater than drag generated by bed friction (Edwards et al., 2004; Warner et al., 2013). Furthermore, Warner et al. (2013) showed that the presence of form drag produces elevated values of C_D, when it is estimated from the depth-averaged along-stream momentum balance.

In literature, less attention has been paid to understanding the shape of the vertical profiles of horizontal velocity during the remaining phases of the tide (namely during early and late ebb and flood). An interesting feature, described for several estuaries, is the occurrence of a mid-depth velocity maximum during flood (e.g. Jay and Smith, 1990; Lacy and Monismith, 2001; Warner, 2005; Chant et al., 2007), which has also been observed in a modeling study of the Chesapeake Bay (Li and Zhong, 2009). This velocity maximum occurs at the upper boundary of the bottom boundary layer (Chant et al., 2007). Cudaback and Jay (2001) explained the occurrence of a mid-depth velocity maximum during early flood in the Colombia inlet, which is a strongly-stratified estuary, using a simple three-layer model based on the barotropic and baroclinic pressure gradient and bed friction. They concluded that bed friction and a strongly-stratified water column are crucial in driving a mid-depth jet. Similar observations in the stratified North Sea were explained by Maas and van Haren (1987) using a comparable model.

To complicate matters further, the shape of the vertical profiles of instantaneous and residual currents varies spatially due to bathymetric and nonlinear effects, as e.g. tidal asymmetry (Aubrey and Speer, 1985; Speer and Aubrey, 1985; Dronkers, 1986; Friedrichs and Aubrey, 1988). Li and O'Donnell (1997) demonstrated that a lateral water depth gradient produces a tidally-driven horizontally-sheared exchange pattern, whereas Li and O'Donnell (2005) showed that the length of an estuary determines the inflow and outflow patterns at the channel and shoals. Scully and Friedrichs (2007) observed lateral asymmetries in current magnitude and concluded that spatial asymmetries in mixing modify the duration of the ebb phase and change the residual circulation. In the Marsdiep basin, the tidal asymmetry is great and is spatially variable. Zimmerman (1976b), Ridderinkhof (1988) and Buijsman and Ridderinkhof (2007a) observed stronger flood currents and inflow at the shallower south side of the Marsdiep tidal inlet and stronger ebb currents and outflow at the deeper north side.

In the Dutch, German and Danish Wadden Sea, the mechanisms that contribute to the residual circulation are still a matter of debate (Zimmerman, 1986; Ridderinkhof, 1988; Buijsman and Ridderinkhof, 2007a; Burchard and Hetland, 2010; Becherer et al., 2011; Flöser et al., 2011). The first three studies argue that tide-topography interaction is the major forcing of residual currents in the Wadden Sea, whereas the latter three argue that tidal straining, and the presence of an estuarine circulation, is the major forcing. Since the shape and variability of the vertical profiles of along-stream velocity are essential for estuarine dynamics, the aim of this paper is to explain the structure (and variability) of the vertical profile of the horizontal velocity in the main channel of the Marsdiep basin. This study shows that the shape of the vertical profiles in the Marsdiep deviates in several ways from the standard estuarine profiles.

Three deployments of a bottom frame in the Marsdiep basin, equipped with an upward-looking Acoustic Doppler Current Profiler (ADCP) and temperature, conductivity and depth sensors (microCAT), resulted in over 100 days of current data during 3 different seasons. This dataset, in combination with simulations with the General Ocean Turbulence Model (GOTM) provides a better understanding of the factors that determine the shape of the vertical profiles of along-stream velocity in the Marsdiep. Hereby, we focus on the combined effects of bed friction and density-related processes, e.g. the baroclinic pressure gradients and vertical stratification, on the vertical profile of along-stream velocity over the tidal cycle. In addition, the mechanism behind the occurrence of a mid-depth along-stream velocity maximum during late flood is investigated. This phenomenon is related to the occurrence of vertical stratification during late flood, which is generated by cross-stream tidal straining and which the small currents are not able to destroy during this phase of the tide. We hypothesize that vertical stratification inhibits the vertical momentum exchange in upward and downward direction, thereby producing the greatest current around the pycnocline: vertical stratification restricts bed-generated turbulence to the lower part of the water column limiting seabed-induced vertical mixing of momentum, whereas the superimposed effect of the barotropic and baroclinic components of the tide limits the increase in current speed with depth, as described earlier, to the part of the water column above the pycnocline.

The paper is structured as follows. In Section 2, more detailed information on the study area, the data handling as well as the model settings is presented. Sections 3 and 4 describe the observations and model simulations, respectively. In Section 5, typical characteristics of the vertical current structure at the study site are discussed in more detail, and in Section 6 the main findings of this study are summarized.

2. Study site, material and methods

2.1. Study site description

The study site is located in one of the main channels of the Western Dutch Wadden Sea, the Texelstroom channel (Fig. 1b). The Western Dutch Wadden Sea is comprised of the Marsdiep and Vlie basins (Fig. 1a) and there is only limited exchange between both basins (Zimmerman, 1976a, 1976b; Buijsman and

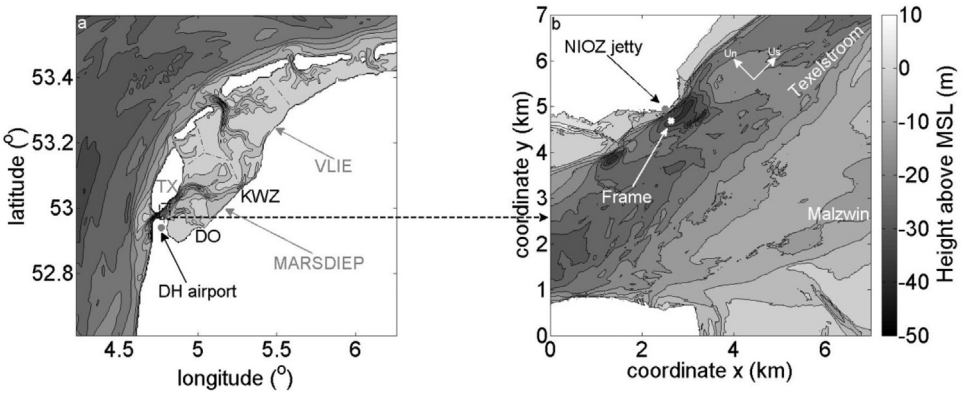

Fig. 1. (a) Bathymetric map of the Western Dutch Wadden Sea (Data source: Rijkswaterstaat, reference mean sea level, MSL) and, in detail, (b) the study site with the location of the bottom frame. The northern (southern) channel is the Texelstroom (Malzwin). To the east, these channels are separated by the tidal flat, Lutjeswaard. DO (KWZ) indicates the location of the fresh water sluices at Den Oever (Kornwerderzand). The gray dots indicate the location of the NIOZ jetty and the Den Helder airport. The reference frame in the zoom-in (b) is a Cartesian coordinate reference frame with the origin in the southwest corner. The resolution of the zoom-in map of the study area is 20 m. The direction of the along-stream (Us) and cross-stream (Un) velocity components are indicated by the white arrows in (b).

Ridderinkhof, 2007b). The main channel, the Texelstroom, is located in the Marsdiep basin where a smaller channel, the Malzwin, is located to the southeast (Fig. 1b). The Texelstroom channel is oriented in approximately westsouthwest-eastnortheast (along-channel) direction and the water depth varies between 10 and 35 m (Fig. 1b). At the study site, the bathymetry is characterized by a sloping seabed with shallower water depths in southwestward direction. The slope in this along-channel direction is approximately 0.013. In addition, up-estuary the water depth decreases again by approximately 20 m (Fig. 1b). Sandwaves are a common feature in this area (Buijsman and Ridderinkhof, 2008a), but a multibeam survey of the study site showed that none are present at the location of the bottom frame (not depicted).

The tides along the Dutch coast and in Marsdiep basin are semi-diurnal with a tidal range of approximately 1 and 1.5 m at the NIOZ jetty during neap and spring tide, respectively (Fig. 3d–f). The vertically-averaged current amplitude varies between 1.2 and 1.8 m/s for neap and spring tide conditions, respectively (Fig. 3a–c). The Marsdiep inlet is characterized by stronger peak ebb than peak flood currents at the southern side, whereas the reversed pattern is observed at the northern side of the inlet (Buijsman and Ridderinkhof, 2007a). This tidal asymmetry results in a net inflow into the basin at the southern side and a net outflow at the northern side. Buijsman and Ridderinkhof (2007a) observed that the friction velocity, roughness length and drag coefficient during one single peak ebb and flood of a neap and spring tide, at the center of the Marsdiep inlet, displayed an ebb-flood asymmetry as well, but they did not explain these differences or their implications to the vertical current structure. They observed greater peak flood friction velocities, roughness lengths and drag coefficients, which suggests greater vertical mixing during flood.

The two major sources of fresh water in the Marsdiep basin are the outlet sluices at Den Oever (DO) and Kornwerderzand (KWZ), which only discharge fresh water from lake IJssel into the Wadden Sea during low water (Figs. 1a and 2). The distance between the sluices at DO and KWZ and the NIOZ jetty is approximately 18 and 37 km. The discharge data is provided by the Dutch governmental agency for infrastructure, Rijkswaterstaat. For more information

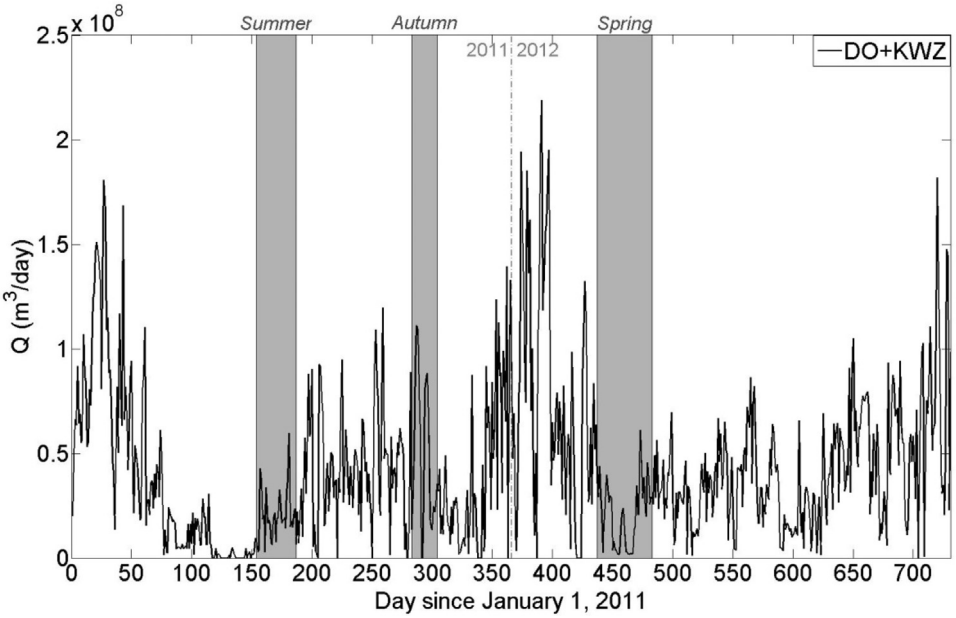

Fig. 2. Sum of daily fresh water discharge at Den Oever and Kornwerderzand during 2011 and 2012. The two years are separated by the dotted gray vertical line. Day 1 represents January 1, 2011. The gray areas indicate the deployment periods, *Summer*, *Autumn*, *Spring*.
Data source: Rijkswaterstaat.

on the computation of the discharge rates and other minor fresh water sources is referred to Duran-Matute et al. (2014) and De Vries et al. (2014), respectively. Based on observed salinity distributions, it has been assumed that two-thirds of the fresh water from the sluices of KWZ are flushed into the North Sea via an adjacent tidal basin, the Vlie basin (Zimmerman, 1976a, 1976b); the other one-third originating from KWZ is assumed to be discharged through the Marsdiep basin, via the Texelstroom channel. All the fresh water from DO is assumed to be discharged through the Marsdiep basin via the Malzwin channel (Zimmerman, 1976a, 1976b). The discharge patterns of the outlet sluices display a strong seasonality with high discharges between October and April and low discharge between May and September (Fig. 2). As a result, the water column is weakly stratified up to 6 psu during slack tides, whereas the currents mix the entire water column during peak currents (De Vries et al., 2012). Interestingly, no modulation of the strength of vertical stratification by the spring neap tidal modulation has been observed, as discussed by De Vries et al. (2012).

The Ekman ($Ek = A_z/(fH^2)$) and Kelvin ($Ke = B/R_i$) numbers can be used to indicate the importance of basin width, friction and Earth's rotation for the exchange flow patterns in estuaries (e.g. Valle-Levinson, 2008), where A_z ($\sim$0.1 m^2/s) is the eddy viscosity, f (1.16×10^{-4} s^{-1} at 53 °N) the Coriolis frequency, H (25 m) the water depth, B (4 km) the width of the channel and R_i (3×10^3 to 10^4 m) the internal Rossby radius ($R_i = \sqrt{g'H}/f$, g' being the reduced gravity). The latter indicates at which length scale rotation becomes important and is defined as the ratio between the internal wave speed and the local Coriolis frequency. Most values are obtained from Buijsman and Ridderinkhof (2008b) and De Vries et al. (2014). It results in conservative estimates of the Ekman and Kelvin numbers of 1.4 and 0.4–1.3, suggesting that the estuary is characterized by strong frictional effects and that the Earth's rotation is usually of minor importance for the exchange flow patterns at the inlet.

2.2. Data collection and instrumentation

A 1.25 m-high bottom frame, equipped with an upward-looking Acoustic Doppler Current Profiler (ADCP) and a conductivity, temperature, depth sensor (microCAT), was deployed (and retrieved) at the north side of the Texelstroom channel on three occasions (Fig. 1b). The bottom frame was placed on the seabed in approximately 32 m water depth, and at a distance of approximately 200 m from the Texel coast and approximately 300 m southeast of the NIOZ jetty.

Characteristics of each deployment are given in Table 1. Each deployment is named after the season which covers the largest timespan of the deployment period, viz *Summer*, *Autumn* and *Spring*. The bottom frame was not equipped with a microCAT during the *Summer* deployment, because the survey was only focused on measuring the velocity. Besides the measurements from the bottom frame, 13-hours anchor station surveys with the R.V. Navicula were conducted next to the location of the frame, measuring amongst others current velocity, conductivity and temperature. This study focuses on the data measured at the bottom frame. The anchor station data from the R.V. Navicula provides an overview of the conditions at the study site since it contains information on the vertical profiles of salinity, which are not available for the bottom frame dataset. A detailed discussion on the instrumentation and data-processing of the shipboard data is already given in De Vries et al. (2014) and is therefore excluded from the present paper.

To measure the flow velocity, the bottom frame was equipped with a four-beam 1.2 MHz RDI Workhorse Monitor ADCP with a beam angle of 20° relative to the vertical. The conductivity, temperature and depth (CTD) was measured with a Sea-Bird Electronics 37-SM MicroCAT. The top of the ADCP was located approximately 30 cm higher than the top of the microCAT sensor. The specific height of the frame was chosen to prevent the frame and sensors from being covered by sand as a result of the high bedload and bedform transport in the region.

The ping rate of the ADCP was set to 0.43 Hz and ensembles were recorded every 30 s containing 10 pings. The bin size was set to 0.5 m, the number of bins to 79 and the blanking distance to 0.5 m. Therefore, the ADCP could effectively cover a range in water depths between 2 and 32 m above the bottom. The velocity data were stored in Earth coordinates (east–west, north–south velocities). In addition, the ADCP send out one 'bottom' ping per ensemble to detect the echo of the water surface. The SBE 37-SM MicroCAT recorded one sample of conductivity, temperature and depth every 30 s.

At the NIOZ jetty (Fig. 1b), the near-bottom pressure was measured at 2.9 Hz by a calibrated Keller 46 pressure sensor. The pressure was converted real-time into sea surface elevation. Sea surface elevation was recorded every minute with an accuracy of 3 cm based on the median of 175 samples. The surface conductivity and temperature were measured by a calibrated Aanderaa conductivity and temperature 3211 sensor. The data were recorded every 12 seconds by an Anderaa 3634 datalogger. The salinity was computed using the Practical Salinity Scale 78 (PSS-78, (Fofonoff, 1985)).

2.3. Data processing

First, the erroneous velocity data of the ADCP above the water surface were excluded by removing all data above the height of the surface echo. Then, the data were rotated from east–west and north–south velocity components to an along-stream and cross-stream velocity component, defined as the direction of maximum and minimum variance of the depth-averaged horizontal velocity vector, respectively. The pitch and roll of the ADCP varied in time (on a timescale from days to weeks) due to morphological change of the seabed, but were almost always below 15°. The only exception occurred between Day 7 and 15 of the *Autumn* deployment, when the pitch was 16°. A visual inspection of the velocity data showed no anomalous small-scale velocity fluctuations, i.e. the vertical profiles resembled the classical law-of-the-wall profiles, and therefore the data was included in the analyses. However, the upper 5 m of the water column displayed velocity variations due to strong orbital wave velocities. To exclude the instantaneous effect of waves on the current, the upper 6 m were

Table 1
Characteristics of the *Summer*, *Autumn* and *Spring* deployment. In addition, the median of the tidally-averaged along-stream salinity gradient obtained from Eq. (1) for each deployment and the date of the 13-hours anchor stations (AS) discussed in Section 3.1 are given.

Name	Start day	End day	Total days	microCAT	$\langle \partial s/\partial x \rangle 10^{-4}$ (psu/m)	AS date
Summer 2011	June 3	July 6	34.1	No	0.3	June 22
Autumn 2011	October 10	October 31	21.9	Yes	2.3	October 17
Spring 2012	March 12	April 27	47	Yes	1.8	March 10

removed. Only the lower 27.25 m of the water column were included in all analyses. Therefore, any side-lobe interference is implicitly excluded from the analyses.

The output data of the microCAT were already given in salinity (psu), potential density anomaly (sigma-theta, kg/m^3), temperature (ITS-90, °C) and depth (m), which is computed internally with the standard Seabird software.

In order to include only complete tidal cycles in the analysis, all data before and after the first and last slack tide were removed. The sea surface elevation (SSE), salinity and wind data were interpolated at 30 s intervals to produce a collection of synoptic datasets.

2.4. Analyses

2.4.1. Data analysis

First, characteristics of the vertical current structure are investigated by computing ensemble-averaged vertical profiles of along-stream velocity. Since the duration and shape of the vertical profiles differ per tidal cycle, the tidal phase (i.e. the timing of early, peak, late ebb and flood and the slack tides) is better approximated by the depth-averaged velocity than by phase or time from a fixed moment of reference. Therefore, an average vertical profile of along-stream velocity is computed per averaging interval of 0.1 m/s of the vertically-averaged velocity, e.g. between 1.0 and 1.1 m/s, similar to e.g. Stacey (2003) and Stacey and Ralston (2005). All the vertical profiles of along-stream velocity within each bin of 0.1 m/s of the depth-averaged current are selected and are averaged to obtain an average vertical profile. A 0.1 m/s interval of the vertically-averaged velocity produced both stable average vertical profiles and an adequate resolution of the tidal cycle. Within each bin, no profiles were excluded from the analysis. When an average profile was based on less than 20 profiles, it was considered not representative enough and was excluded from the analysis. This threshold resulted in the exclusion of 5 velocity bins at the outer limits of the velocity range. The number of velocity profiles varied between 24 and 8200 per bin with an average of 2300 velocity profiles. Differences between the deployments reflect temporal variations in forcing conditions. The analysis focuses on the vertical structure of the along-stream velocity.

This approach provides a clear picture of the first order variability of the vertical profile over one tidal cycle and between the seasons. However, the second order effects around slack tide as a result of the asymmetry of the tide are neglected, because the vertical profiles of the early and late ebb and flood phase fall within the same bin of the depth-averaged velocity. These effects are investigated by computing average vertical profiles from peak ebb to peak flood and vice versa (EtoF and FtoE, respectively).

Second, the structure of the vertical profile under a varying salinity gradient is investigated in Section 3.3 by analyzing the relationship between the vertical shear in along-stream velocity and the along-stream salinity gradient, $\langle \partial s/\partial x \rangle$ over two tidal cycles, as indicated by the brackets. The latter is approximated by a frozen field assumption (Stacey et al., 2010).

$$\left\langle \frac{\partial S}{\partial x} \right\rangle = 2\pi \frac{S_{rms}}{L}, \tag{1}$$

where S_{rms} is the root-mean-square of salinity and L ($=u_{\mathrm{rms}}T$) is the tidal excursion length based on the root-mean-square of the depth-averaged along-stream velocity and the tidal period. The salinity was measured either at the bottom frame (*Autumn* and *Spring*) or, if the former was not available, at the NIOZ jetty (*Summer*). Stacey et al. (2010) mention this method is more robust than the local advective calculation of the salinity gradient, because the latter is invalid in regions where lateral advection is important, as is the case in the Marsdiep basin, as this study will show. The computed values of $\langle \partial s/\partial x \rangle$ correspond well with the observed values discussed in De Vries et al. (2014) and provide a method to relate the variation in salinity gradient, i.e. density gradient, to the shape of the vertical current structure. The $\langle \partial s/\partial x \rangle$ ignores any information on the direction of the gradient.

Third, to investigate the impact of bed friction on the current structure, the drag coefficient can be computed using either direct stress estimates or logarithmic fits of vertical profiles of along-stream velocity. With the available data, only the latter approach is possible. This technique is discussed in more detail in e.g. Lueck and Lu (1997). The logarithmic law-of-the-wall generally represents the lower part of the water column well provided the water column is well-mixed. In that case, an estimate of the friction velocity, u_* (m/s), and roughness length, z_0 (m) is obtained from fitting the logarithmic profile:

$$u(z) = \frac{u_*}{\kappa} \ln \frac{z}{z_0}, \tag{2}$$

where u is the along-stream velocity (m/s), z is the height above the bottom (m), and κ is the von Karman constant (0.41) to the observed current structure. The lowest 10 m of the water column are used to obtain the roughness height and friction velocity through a least-squares fit of the vertical profiles. Up to this height above the bottom, the R^2 of the logarithmic fits were good, being greater than 0.95.

An estimate of C_D, based on u_*, is obtained using the bed shear stress, τ_b, given by

$$\tau_b = \rho u_*^2, \tag{3}$$

and the empirically-proven assumption that the shear stress in the lowest part of the water column ($0.1H$) is constant and equals the bed shear stress (van Rijn, 2011). The drag coefficient is then computed by

$$C_D = \frac{u_*^2}{U_b^2}, \tag{4}$$

where u_b is a reference velocity, here at 2 m height above the bottom (hab). The drag coefficient represents the slope of a least-squares fit between the values of ${u_*}^2$ and ${u_b}^2$ (e.g. Geyer et al., 2000; Fong et al., 2009). The u_* and u_b are computed every 10 min of each dataset based on the nearest 8 ensembles. A bootstrap, i.e. resampling method with 100 samples is used to compute the standard error and affirms the reliability of the computed drag coefficients. Other studies (e.g. Geyer et al., 2000; Fong et al., 2009) used a reference velocity at 1 m hab. Consequently, the values presented in this study underestimate with respect to previous studies, because the along-stream velocity is greater at 2 m hab.

2.4.2. Numerical model set-up

To understand the mechanisms that determine the shape of the vertical profiles of along-stream velocity, (semi-)idealized, and (highly-simplified) semi-realistic model simulations were run with the General Ocean Turbulence Model (GOTM, http://www.gotm.net/). An overview of the model runs is given in Table 2. The goal of the former is to identify the important (along-stream) hydrodynamic processes at the study site, assuming a sinusoidal tidal cycle, a constant salinity gradient and a constant bottom roughness. The goal of the latter is to determine and explain the observed shape of the vertical profiles at the study site by incorporating velocity data from the *Spring* deployment.

The numerical model GOTM is an open source state-of-the-art one dimensional water column model, which includes a variety of vertical mixing parameterizations (Burchard and Baumert, 1995;

Table 2
Overview of the conditions of the numerical simulations (run 1–9). The simplified and semi-realistic simulations are discussed in Sections 4.1 and 4.2, respectively. The idealized runs are characterized by a sinusoidal tide. The conditions of the semi-realistic scenarios indicate neap or spring tide conditions. The other parameters given are the water depth, *H*, the along-stream tidal current, along Us, the along-stream salinity gradient, ds/d*x*, the top-to-bottom salinity difference, Δ*S*, the input of the cross-stream currents, cross Un, and the cross-stream salinity gradient, ds/d*y*. The semi-realistic runs are fored by data input. The $Z=2$ m indicates that the simulation is forced by the near-bed along-stream velocity. VP indicates that the model is forced by the entire observed vertical profiles of velocity.

	Run 1	Run 2	Run 3	Run 4	Run 5	Run 6	Run 7	Run 8	Run 9
Conditions	Sine	Sine	Sine	Neap	Neap	Spring	Spring	Neap	Spring
***H* (m)**	30	30	15	30	30	30	30	30	30
Along Us (m/s)	1.2	0.8	0.8	$Z=2$ m	$Z=2$ m	$Z=2$ m	$Z=2$ m	*VP*	*VP*
ds/d*x* (10^{-4} psu/m)	−2	−2	−2	−2	−2	−2	−2	−2	−2
Δ*S* (psu)	0	0	0	0	1	0	1	0	0
Cross Un (m/s)	–	–	–	–	–	–	–	*VP*	*VP*
ds/d*y* (10^{-4} psu/m)	–	–	–	–	–	–	–	−2	−2
	Idealized			Semi-realistic					

Burchard et al., 1998; Burchard and Bolding, 2001). The one-dimensional dynamical horizontal momentum equations, neglecting advection, Coriolis and curvature terms are (Burchard, 2009; Burchard and Hetland, 2010):

$$\frac{\partial u}{\partial t} - \frac{\partial}{\partial z}\left(A_z \frac{\partial u}{\partial z}\right) = - z\frac{\partial b}{\partial x} - p_g^x(t), \tag{5}$$

$$\frac{\partial v}{\partial t} - \frac{\partial}{\partial z}\left(A_z \frac{\partial v}{\partial z}\right) = - z\frac{\partial b}{\partial y} - p_g^y(t), \tag{6}$$

and the buoyancy equation, which includes advection is

$$\frac{\partial b}{\partial t} + u\frac{\partial b}{\partial x} + v\frac{\partial b}{\partial y} - \frac{\partial}{\partial z}\left(K_z \frac{\partial b}{\partial z}\right) = 0, \tag{7}$$

where x, y and z are the along-stream, cross-stream and vertical coordinate, respectively, and u, v, b, A_z and K_z are the along-stream velocity, cross-stream velocity, buoyancy, the eddy viscosity and eddy diffusivity, respectively. The along-stream and cross-stream barotropic pressure gradients are indicated by $p_g{}^x$ and $p_g{}^y$. The second-order turbulence model of Canuto et al. (2001) was used. A comparative study of four turbulence closure models by Burchard and Bolding (2001) showed that this turbulence model performed best.

The first and second term on the right hand side of (Eqs. (5) and 6) represent the baroclinic and barotropic pressure gradients, respectively. The buoyancy is defined as

$$b = - g\frac{\rho - \rho_0}{\rho_0}, \tag{8}$$

where g is the gravitational acceleration, ρ is the density and ρ_0 is the constant reference density (1000 kg/m^3). The magnitude of the salinity gradient used as a model forcing is -2×10^{-4} psu/m, which is the same order of magnitude as the conditions in *Autumn* and *Spring,* and corresponds with observations in De Vries et al. (2014).

The barotropic pressure gradient function, $p_g{}^x$, is computed based on a simplification from the three-dimensional to the one-dimensional hydrostatic equations as described and validated in Burchard (1999) using information of the temporal derivative of velocity at one single point. It enables the computation of the barotropic pressure gradient based on a timeseries of velocity at one single location. For the idealized model simulations, the velocity is defined as a sinusoidal tidal wave with a period, T, of 12.5 h:

$$\bar{u}(t) = \frac{1}{H}\int_{-H}^{0} u(z,t)\mathrm{d}z = U\cos\left(2\pi\frac{t}{T}\right). \tag{9}$$

The barotropic pressure gradients in the semi-realistic model scenarios are based on the velocity input from the *Spring* deployment. The technique to compute the barotropic and baroclinic pressure gradients assumes homogeneity along the x and y directions. Bathymetric variations are therefore not incorporated in the model. The incorporation of velocity data in the semi-realistic model implicitly includes environmental factors such as the bed slope.

All scenarios except run 3 are run in a water depth of 30 m, consisting of 100 layers. A time step of 10 s is chosen with an output resolution of 10 min. The results of the model output are insensitive to variations in time step. The bulk flow properties are the molecular viscosity and diffusivity and the formulation of the equation of state. The physical bottom roughness is set to 0.05 m. A relaxation time of 10,800 s is specified (3 h) for the bulk flow of salinity (e.g. Verspecht et al., 2009). To keep the model stable, a relaxation time is imposed for when the bulk salinity deviates from the initial conditions. Verspecht et al. (2009) found that 3 h provided stable model results. Since density variations are mainly determined by salinity, the temperature field is excluded. Advection of salinity is always permitted. The upper part of the water column, which is influenced by the intra-tidal in-situ water level fluctuations, and also the effect of wind stress is ignored, because these processes are considered of minor importance to the overall characteristics of the current structure.

The idealized scenarios (runs 1–3, Table 2) are characterized by a sinusoidal tidal velocity as described above, where the amplitude is varied between 0.8 and 1.2 m/s. In addition, the water depth is also varied. The salinity gradient is kept constant to -2×10^{-4} psu /m.

The first four semi-realistic scenarios are forced by the measured along-stream velocity at 2 m above the bed from the *Spring* deployment (runs 4–7, $Z=2$ m in Table 2). Runs 4–7 are forced by an along-stream salinity gradient of -2×10^{-4} psu/m and advection of salinity is permitted. An additional vertical stratification of 1 psu during the onset of flood is imposed for run 5 and 7, which is allowed to develop over the tidal cycle. Runs 4 and 6 are characterized by well-mixed conditions of 28 psu, whereas the salinity profiles of runs 5 and 7 consisted of 27 psu in the upper 10 m and 28 psu in the upper 10 m of the water column. In the middle 10 m, the water column was continuously-stratified. The well-mixed and weakly-stratified conditions correspond with the conditions observed at the study site as discussed in Section 3.1.

The $p_g{}^x$ is forced by the vertical profiles of along-stream velocity for runs 8 and 9. So far, the cross-stream dimension of the barotropic and baroclinic terms has been neglected. In runs 8 and 9 of the semi-realistic model simulations, $p_g{}^y$ is also forced by the observed vertical profiles of the cross-stream current. In addition, a constant lateral salinity gradient is imposed in order to investigate the effect of cross-stream processes on the generation of

vertical stratification and on the shape of the vertical profile of along-stream velocity. The results of the model simulations are discussed in Section 4.

3. Observations

3.1. Current and salinity characteristics

The temporal and vertical information of currents and salinity obtained from the bottom frame and 13-hours anchor station measurements provide us with an overview of the intra-tidal and seasonally variable conditions at the study site.

During the periods of data collection, the tidal amplitude (Uamp) and sea surface elevation (SSE) are mainly determined by the spring neap tidal cycle and the wind conditions (Fig. 3a–f). In *Summer*, variations in Uamp and SSE component by the spring neap tidal cycle are small but discernible (Fig. 3a, d, and j). The tidal amplitude is greater during spring tide than during neap tide. Between Days 290 and 293 of *Autumn*, a major storm event induced significant variations, which distorted the spring neap tidal modulation (Fig. 3b, e, and k). In *Spring*, wind-induced variations in SSE component are small (Fig. 3c, f, and l). A clear spring neap tidal modulation is visible during the first 30 days, which is smaller from Day 365.

The low discharges at DO and KWZ the month prior to the *Summer* deployment (Fig. 2) resulted in a high average salinity of around 32 psu during the first 27 days of the deployment (Fig. 3g). Only small tidally-driven fluctuations were superimposed on the average salinity. The intra-tidal fluctuations increased during the last 6 days of the measurement period. On the last day, the salinity dropped by 5 psu due to a northeasterly wind in combination with an increase in fresh water discharge from the sluices (Fig. 3g and j). Similar events of decreases in salinity driven by (north)easterly winds occurred between Days 286–289, 297–299 of *Autumn* and Days 457–462 of *Spring*, whereas southwesterly winds resulted in an average increase in salinity, e.g. between Days 291–293 of *Autumn* and Days 441–446 of *Spring* (Fig. 3h, k, i, and l). It suggests a considerable impact of wind dynamics on the flushing rates of the basin. The intra-tidal salinity fluctuations were greatest during *Autumn* and *Spring* (Fig. 3h and i).

The salinity field (Fig. 3g–i) is determined by the fresh water discharge rates prior to each deployment period (Fig. 2). The fresh water discharge from the sluices during the *Summer* deployment is greater than in *Spring* (Fig. 2). However, the mean salinity and the intra-tidal variations in salinity are smaller during *Summer* (Fig. 3g–i). Our data indicate a lag effect of several weeks between the fresh water discharge of the sluices and the salinity variations at the inlet.

The anchor station data in Fig. 4a–c, obtained with the moored Navicula, display a large intra-tidal difference in the strength and duration of the flood and ebb tide. The maximum flood current is reached rather abruptly and only occurs briefly. Generally, the short peak flood is followed by a longer period of weaker flood currents. The currents during ebb are greater than during flood. The variation in depth-averaged current between the anchor stations illustrates the great inter-tidal variability.

In *Summer,* the vertical profiles of along-stream velocity reach their maximum velocity near the surface. Deviations from the logarithmic velocity profile are observed in *Autumn* and *Spring* (Fig. 4d vs 4e and f). Then, a mid-depth velocity maximum is observed during late flood, whereas during ebb the maximum velocities are still near the surface. The mid-depth velocity maximum coincides with the presence of a vertically-stratified water column (Fig. 4j–l) and the occurrence of a cross-stream circulation cell (Fig. 4g–i). In *Summer*, vertical stratification is negligible (< 1 psu). It is greater in *Autumn* and *Spring*, being up to 3 psu. Interestingly, the water column is well-mixed during ebb,

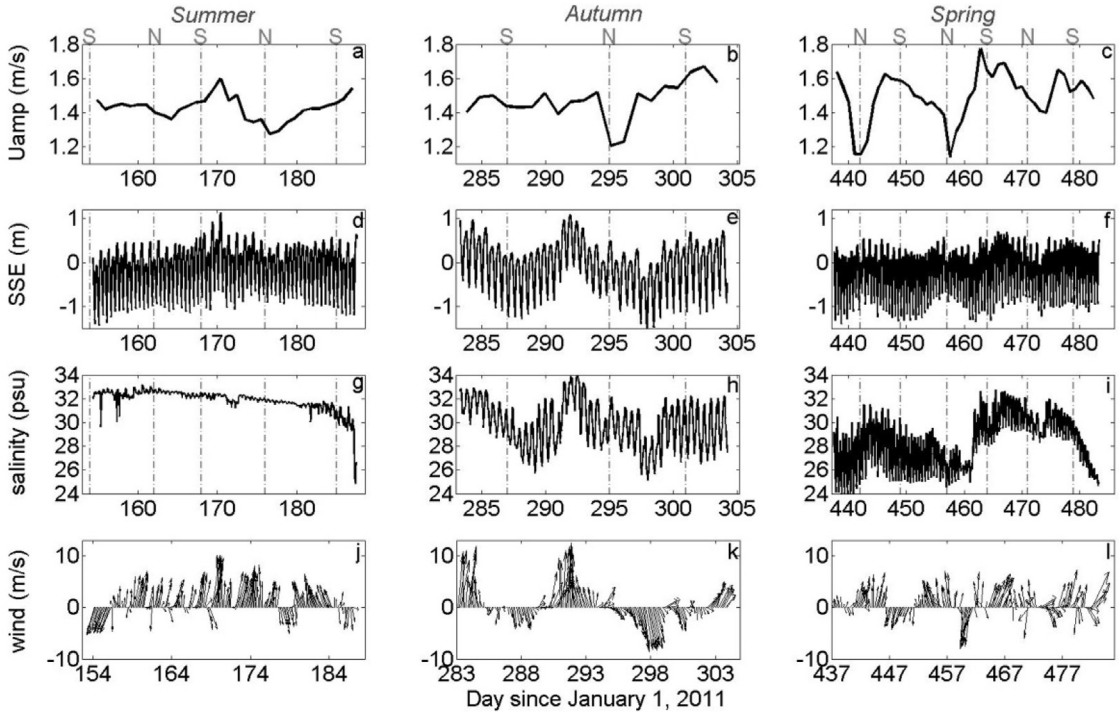

Fig. 3. Depth-averaged tidal amplitude at the bottom frame (Uamp, 1st row), the sea surface elevation (SSE) and salinity at the NIOZ jetty (2nd and 3rd row, respectively) and wind vectors at Den Helder Airport (4th row) during *Summer*, *Autumn* and *Spring* (left, middle and right column, respectively). Uamp is a discrete value and is based on two tidal cycles to remove the diurnal inequality. It is defined as half of the range in depth-averaged current velocities. Wind vectors are oriented in down-wind direction. The spring neap tidal cycle is indicated in gray by N and S at the top and by the dotted gray vertical lines in the panels and is based on astronomical tidal charts. The time is given in days since January 1, 2011.

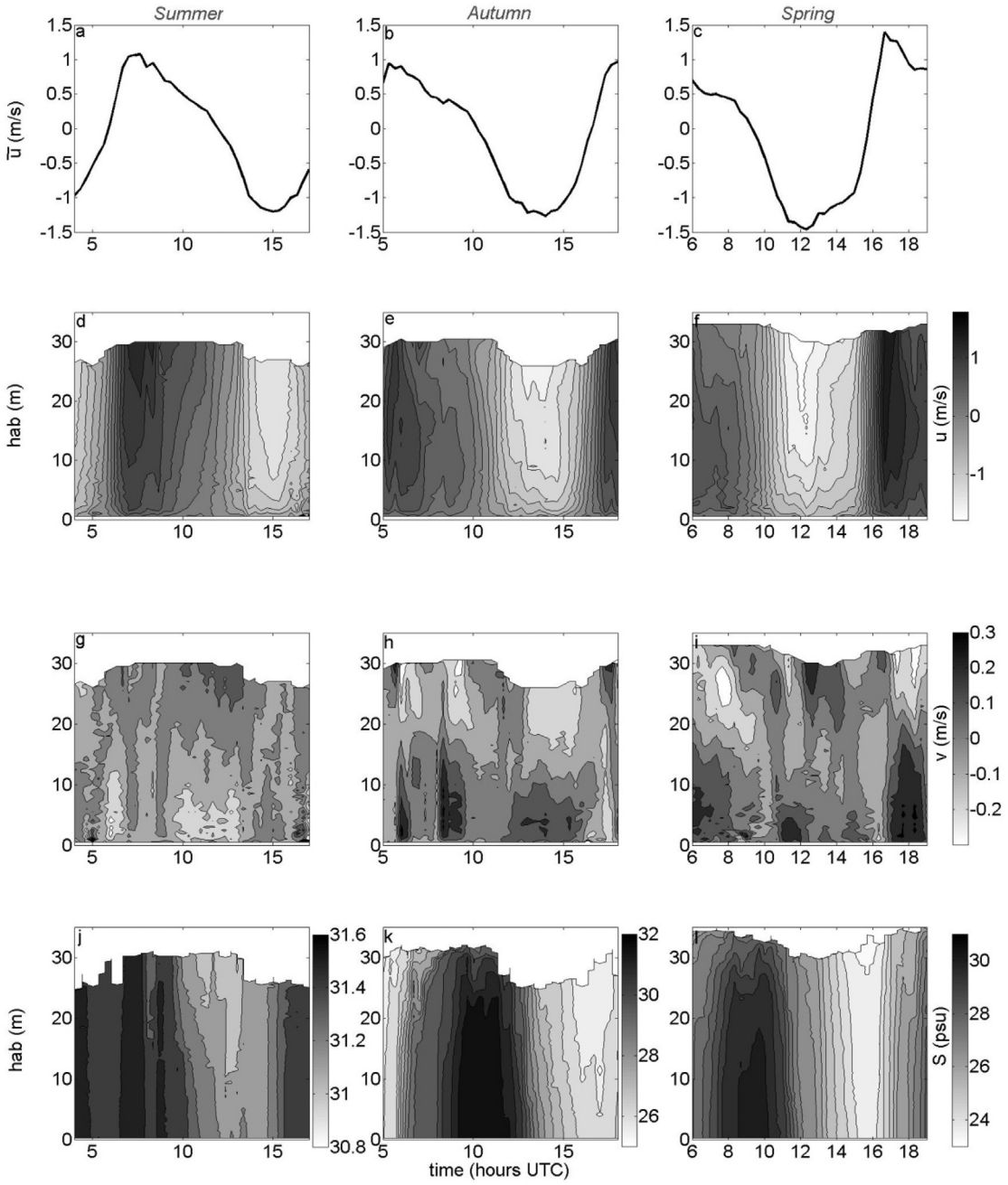

Fig. 4. Overview of anchor station data collected during the three different deployment periods. The seasons are indicated at the top. The first row displays the depth-averaged along-stream velocity, the second and third row the vertical profiles of along- and cross-stream velocity, respectively, and the fourth row the vertical profiles of salinity.

indicating that classical tidal straining is not important at the study site, and the water column is most stratified during late flood and slack before ebb.

The strength of the cross-stream currents varies between and during the tidal cycles (Fig. 4g–i). In *Summer*, the maximum cross-stream currents are only half the magnitude of those in *Autumn* and *Spring*, i.e. 0.15 and 0.30 m/s, respectively, most likely due to a weaker fresh water discharge in the period preceding *Summer* (Fig. 2). The greatest cross-stream currents are present during late flood and peak ebb. Cross-stream circulation cells are present between 6:00–10:00 (late flood) and 13:00–16:00 (peak ebb) hours UTC of *Autumn* and between 17:00–19:00 (late flood) and 12:00–14:00 (peak ebb) hours UTC of Spring. Buijsman and Ridderinkhof (2008b) showed that the cross-stream currents in the Marsdiep inlet are driven by centrifugal and Coriolis acceleration and baroclinic pressure gradients. Furthermore, they conclude that differential advection is important during late flood because the densest flood water enters the Marsdiep basin in the middle of the channel, which creates a lateral density gradient and drives a cross-stream circulation cell. The differential advection mechanism is evident in the observed cross-stream circulation cell of Fig. 4 and its seasonal variability. In the next section, the vertical structure of the along-stream velocity is treated in more detail using the data from the bottom frame deployments.

3.2. Average vertical profiles of along-stream velocity

The average vertical profiles of along-stream velocity as a function of the depth-averaged velocity are depicted in Fig. 5. The

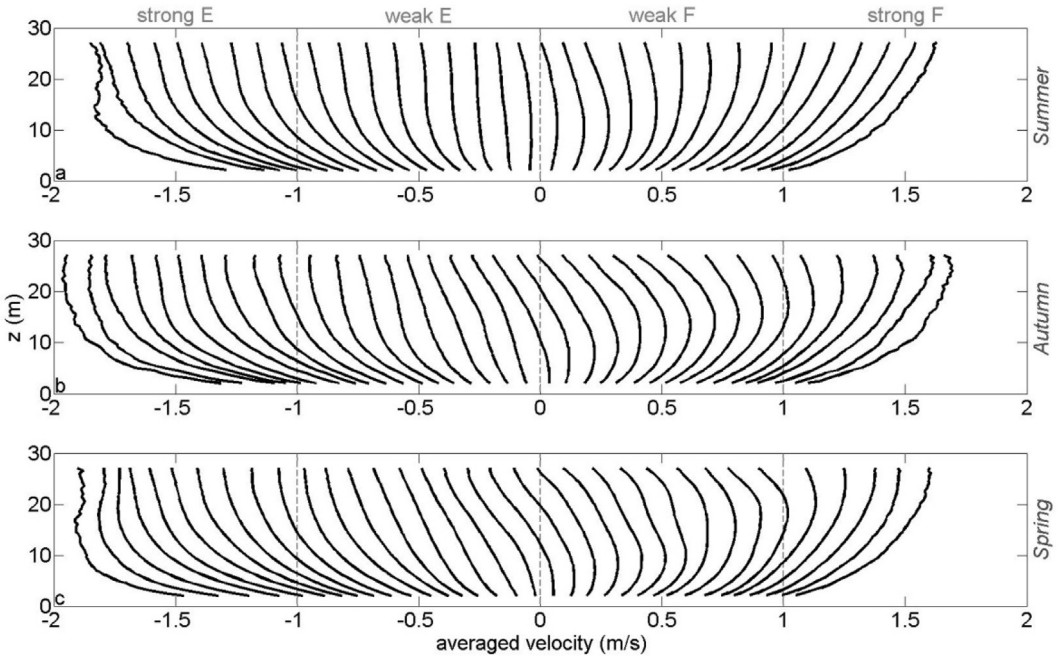

Fig. 5. Average vertical profiles of along-stream velocity per bin of 0.1 m/s of the depth-averaged current for *Summer*, *Autumn*, *Spring*, as indicated at the right of each panel. The *x*- and *y*-axes show the velocity and height above the bed (*Z*). Each black line represents an averaged vertical profile as a function of the depth-averaged current as described in Section 2.4.1. The vertical dashed lines indicate the transition from strong to weak ebb (*E*) and flood (*F*) currents and the location of the slack tide.

x- and *y*-axes represent the velocity and height above the bottom, respectively. Each line represents an average vertical profile, as explained in Section 2.4.1.

The vertical profiles of the strong (>1 m/s) ebb and flood currents deviate substantially from each other (Fig. 5). Strong ebb is characterized by greater vertical gradients in velocity, i.e. shears, in the lower part of the water column compared to strong flood (>1 m/s). The current velocity increases up to approximately 10 m above the seabed for strong ebb, whereas the vertical gradients in velocity are smaller in the lower part of the water column during strong flood. During flood, these vertical shears remain high up to 15–20 m above the seabed. In the upper part of the water column, the velocity profile is more uniform during strong ebb than during strong flood. These patterns contradict the standard estuarine vertical profiles as described by e.g. Jay and Musiak (1996).

Furthermore, the vertical profiles of the weak (<1 m/s) flood and ebb currents differ from the strong currents. During weak ebb, the vertical gradients in velocity are more uniformly distributed over the water column (Fig. 5). During weak flood, the shape of the vertical profiles changes greatly. A mid-depth velocity maximum is observed, modifying the vertical structure of the along-stream velocity during *Autumn* and *Spring* (Fig. 5b and c). Also, the shape of the vertical profiles of the weak ebb and flood currents exhibits seasonal, inter-dataset, variability. The mid-depth velocity maximum during weak flood is better developed under the presence of fresher conditions in *Autumn* and *Spring* (Fig. 3b and c); the mid-depth velocity maximum persists until higher depth-averaged velocities are reached. Higher depth-averaged velocities are characterized by a mid-depth maximum located higher up in the water column. It can be indicative of an intensification of the bottom-generated turbulence in the presence of vertical stratification which is investigated in Section 4.1 using numerical simulations. Weak ebb currents display an increase in vertical gradients of velocity in the upper part of the water column under the fresher conditions in *Autumn* and *Spring*, probably related to the dampening of turbulence by strain induced vertical stratification as was observed for example in the German Wadden Sea (Becherer et al., 2011) and the York River estuary (Scully and Friedrichs, 2007).

Around slack tide, the vertical profiles resemble a tidally-averaged profile of estuarine circulation during *Autumn* and *Spring* (Fig. 5). Weak ebb and flood currents show landward flow at the bottom and seaward flow at the surface. The inter-tidal variability reflects the seasonal fluctuations in baroclinic forcing. In *Summer*, the vertical profiles near slack tide are uniform over almost the entire water column due to the absence of strong density gradients (Table 1 and Fig. 5a), whereas in *Autumn* and *Spring* indications of an estuarine circulation are more apparent due to the presence of higher density gradients during these time periods caused by elevated discharge at the sluices (Fig. 5b and c). The higher baroclinic pressure gradients can modify the vertical profiles during slack tide by enhancing the vertical stratification in the water column and the related vertical shears in along-stream velocity. This could potentially enhance the residual circulation as discussed by Stacey et al. (2001).

To investigate the impact of asymmetric effects on the tide, a distinction is made between the vertical current structure from peak ebb to peak flood (EtoF) and its antagonistic phase (FtoE). The asymmetry in near-bed velocities and vertical shear between ebb and flood are similar for EtoF and FtoE as well as the occurrence of a mid-depth velocity maximum during early and late flood (not depicted). However, the vertical profiles of EtoF and FtoE differ from one other around the slack tides (Fig. 6). In Fig. 6, the *x*-axis of FtoE is reversed in order to accurately represent the temporal propagation of the tide from late flood to early ebb. The onset of the flow reversal from EtoF starts near the seabed due to the effect of bed friction on the flow. Higher up in the water column, frictional effects are smaller and therefore inertial effects dominate and the current reverses later. From FtoE, the flow reversal patterns display entirely different characteristics. The flow reversal begins in the upper part of the water column and ends in the lower part of the water column. During late flood, there is another momentum sink, resulting in the earliest flow reversal in the upper part of the water column, which is greater than the frictional effects of the seabed. A cross-stream circulation cell during late

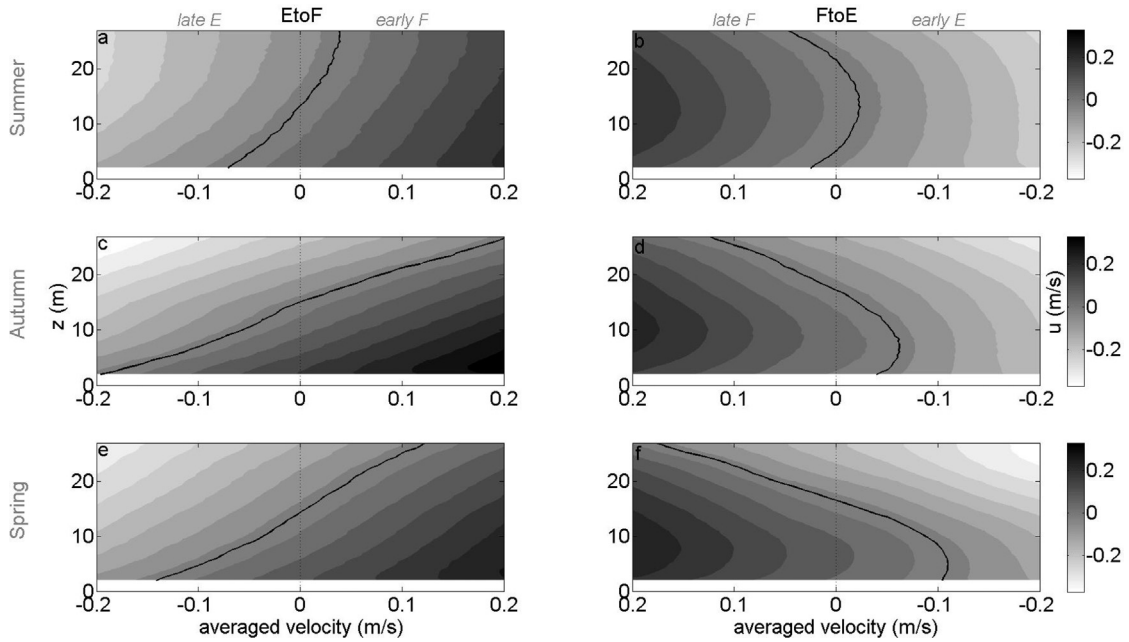

Fig. 6. Vertical profiles of along-stream velocity for the *Summer*, *Autumn* and *Spring* deployment (upper to lower row, respectively) during the slack tides. The slack period from ebb (flood) to flood (ebb), named EtoF (FtoE), is depicted in the left (right) column. Early and late flood (*F*) and ebb (*E*) are indicated at the top in gray. Along-stream velocity is given as a function of the depth-averaged velocity (*x*-axis) and height above the bed (*Z*, *y*-axis). The solid black lines indicate the location where the velocity is 0 m/s, which is a measure of the reversal of the current.

flood, generated by differential advection as illustrated in Fig. 4 and discussed in Section 3.1, is a mechanism which can serve as an additional momentum sink.

Greater density gradients in *Autumn* and *Spring* are accompanied by an enhancement of the patterns described above (Fig. 6c–f). The range of depth-averaged velocities over which the current reverses direction is greater than in *Summer*. The slower reversal from EtoF with respect to *Summer* might be indicative of the greater vertical stratification that is generated by the large density gradients, which dampens the vertical momentum exchange and delays the onset of the flood tide, as was already discussed by Scully and Friedrichs (2007).

The median duration of the slack tides, defined as the time period when the along-stream current is not unidirectional over the vertical profile, is much smaller from EtoF than from FtoE, being between 10–17 and 43–61 min, respectively (Fig. 6). The duration increased from *Summer* to *Autumn* and *Spring*, which suggests that the vertical density gradients influence the duration of the current reversal probably by limiting the vertical momentum exchange. The duration of the current reversal from EtoF is greater in *Autumn* than in *Spring*, whereas the duration from FtoE is greater in *Spring* than in *Autumn*.

Summarizing, the vertical gradients in along-stream velocity in the lower part of the water column are greater during ebb, whereas they are greater in the upper part of the water column during flood. These patterns deviate from the standard estuarine vertical profiles. The horizontal density gradient, by forcing the strength of the vertical stratification, has a considerable influence on the structure of the vertical profiles, amongst others reflected in the inter-seasonal variability. Around slack tide, the vertical profiles represent an estuarine circulation. The early and late phases of ebb and flood are characterized by similar vertical current structures, but the current reversal around high and low water slack differ markedly from one other.

3.3. Impact of density field on the vertical current structure

To further investigate the impact of the density field on the vertical current structure, the relationship between the calculated salinity gradient, $\langle \partial s/\partial x \rangle$ and the vertical shear in along-stream velocity is analyzed. The shear during different current strengths is compared by tidally-averaging over a range of the depth-averaged along-stream current as given in each panel of Fig. 7. Also, the vertical shear at different heights above the bottom is depicted in each panel, as indicated by the different gray icons. The solid lines are the least-squares linear fits to the shears at each height above the bed. Negative (positive) shear during ebb (flood) signifies increasing current velocities with increasing height above the bed.

High current velocities during ebb and flood are characterized by the greatest shears, $|du/dz|$, close to the seabed (h2.5) for all salinity gradients (gray dotted line, Fig. 7a and b). The vertical shears higher up the water column are small (h15 and h25, dotted black and solid black lines, respectively). For all ebb velocities (Fig. 7a, c, and e), similar patterns are observed characterized by high shears near the bed and small shears higher up in the water column. These patterns resemble the classical logarithmic profiles of along-stream velocity. Furthermore, there is no clear relationship between $\langle \partial s/\partial x \rangle$ and vertical shear, which indicates that the vertical profile is not substantially influenced by the along-stream salinity gradient.

In contrast, the shear of the flood currents does correlate with $\langle \partial s/\partial x \rangle$. Weak flood currents (0.3–0.7 and 0.8–1.2 m/s in Fig. 7f and d, respectively) are characterized by a reversal of the sign of the vertical shear in the upper part of the water column. In Fig. 7d, R^2 is 0.37 and 0.55 for 15 and 25 m above the bed, respectively. In Fig. 7f, the values were 0.3 and 0.66. This reversal in sign of the vertical shear corresponds with the presence of a mid-depth velocity maximum. It evidences a linear relationship between the strength of the salinity gradient and the magnitude of the negative vertical shear, which implies a relationship between the mid-depth velocity maximum and the baroclinic pressure gradient.

3.4. Drag coefficients

The observed near-bed vertical shears in along-stream velocity can be explained by an asymmetry in drag coefficient. Evidence of

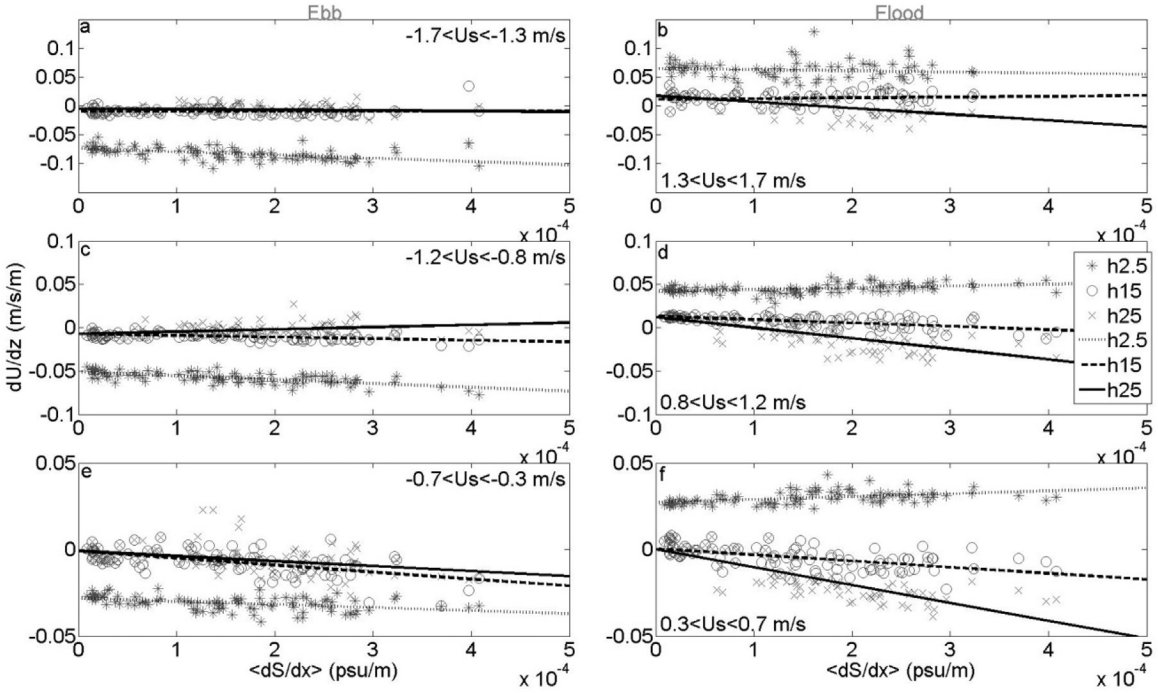

Fig. 7. Vertical shear in along-stream velocity, d*u*/d*z*, during ebb and flood (left and right column, respectively) as a function of the along-stream salinity gradient, ⟨d*s*/d*x*⟩. The shear is computed for different current magnitudes, which are the averages of 1.3–1.7 (upper row), 0.8–1.2 (middle row) and 0.3–0.7 m/s (lower row) of the depth-averaged along-stream velocity. For each individual tidal cycle of all deployments, the vertical shear is computed at 2.5, 15 and 25 m above the bed (*, o and x, respectively), based on the closest 5 bins. The least-squares linear fits correspond to the different heights above the bed, as indicated in the legend.

an asymmetry is given in Fig. 8, which shows the 4-minute averages of u_* and u_b squared as well as the estimates of the drag coefficient. An asymmetry in the drag coefficient between ebb and flood is observed for all deployments. The scatter increases considerably from *Summer* to *Autumn* and *Spring* which suggest that other processes influence the estimation of the drag coefficient under increased baroclinic forcing. The greater variability during *Autumn* and *Spring* (Fig. 8b and c) might be driven by variations in vertical stratification and in cross-stream currents. It is striking that the asymmetry in drag coefficients is very similar for all seasons. The drag coefficient is between 1.5 and 2 times greater during ebb than during flood, which suggests a time-independent

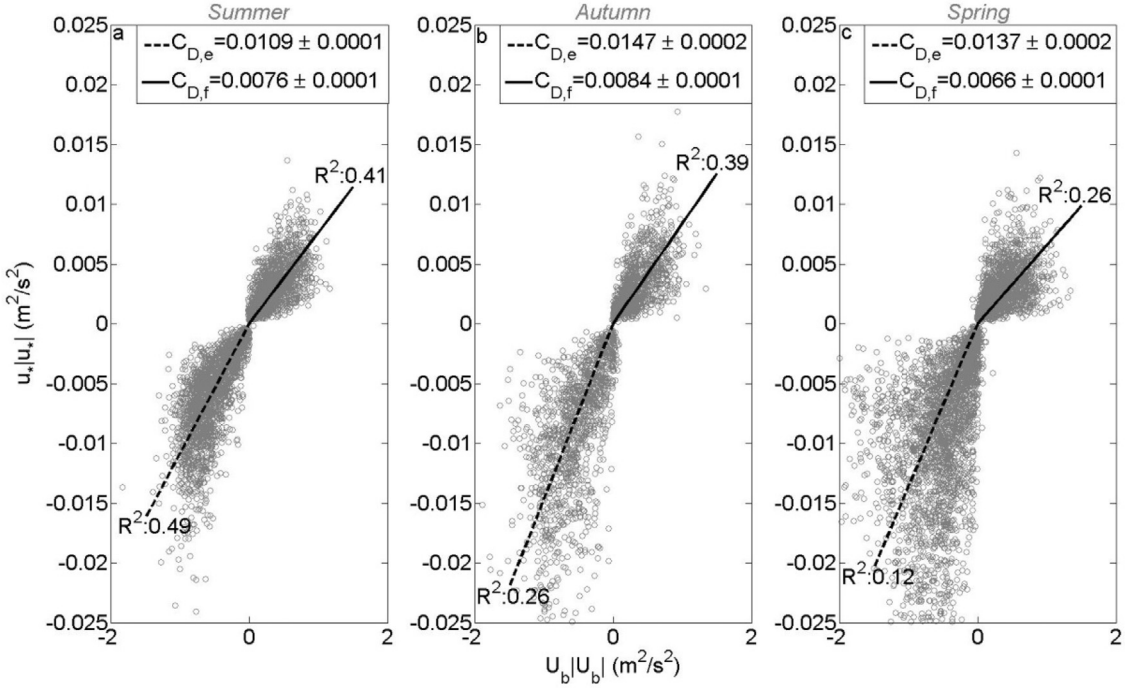

Fig. 8. The relationship between friction velocity, u_*, squared and near-bed velocity, u_b, (at 2 m above the bed) squared for *Summer*, *Autumn* and *Spring* (left, middle and right column, respectively). The gray circles indicate the individual values of the 8-ensembles averages. The dashed and solid lines indicate the least-squares fit to the datapoints for ebb and flood, respectively. The slope represents the drag coefficient, C_D, as given in the legends. The standard error is computed with a bootstrap method and the R^2 of each best-fit are given in each panel.

process, such as e.g. tide-bathymetry interaction by form drag. During peak ebb, the observations deviate from the linear fit with overestimated values of u_*^2 similarly to the observations of Geyer et al. (2000) in the Hudson estuary. Geyer et al. (2000) suggest that other momentum sinks or variations in the stress–velocity relationship might explain this deviation.

The persistent asymmetry in drag coefficient in Fig. 8 is time-invariant under a wide range of conditions. Therefore the variable cross-stream currents and vertical stratification are unlikely factors to explain this asymmetry. The contribution of the cross-stream currents to the modification of the drag coefficient is investigated by removing all data points with near-bed cross-stream velocities greater than 0.1 m/s. It results in only a minor variation in C_D and the asymmetry between ebb and flood remains similar (not shown). Vertical stratification is highly variable in the Marsdiep and might explain the great variability but not the asymmetry itself. Possible explanations for the deviation in near-bed velocities from standard estuarine theory are considered in the discussion.

4. Numerical model simulations

To better understand what determines the vertical structure of along-stream velocity in the Marsdiep, several model scenarios were run with GOTM (Table 2). Idealized runs were used to identify the basic one-dimensional along-stream processes that shape the vertical structure under conditions similar to the study site. Furthermore, the importance of the strong currents and large water depths is evaluated. Dissimilarities between the observations and the idealized model runs indicate the possibility of other important processes. Semi-realistic runs were then applied to understand these characteristic processes.

4.1. Idealized scenarios

To investigate the conditions that are required to generate a mid-depth velocity maximum, idealized scenarios were run. These runs show that the presence of vertical stratification can generate a mid-depth velocity maximum. Furthermore, they show that along-stream tidal straining can only explain a mid-depth velocity maximum during early flood since the peak flood currents mix the entire water column.

The tidal amplitude of 1.2 m/s in run 1 produces a well-mixed water column with the maximum velocities near the surface during nearly the entire tidal cycle (Fig. 9a, d, and g). A small increase in vertical stratification is observed in the upper part of the water column during the early flood phase, which is driven by along-stream tidal straining. The weak stratification during early flood is already capable of generating a small mid-depth maximum (Fig. 9a).

The smaller amplitude of run 2 results in the presence of a mid-depth velocity maximum during the entire flood phase (Fig. 9b), because the peak currents lack sufficient kinetic energy to mix the entire water column. Therefore, vertical stratification is generated at 15–20 m above the bed. Also, the average vertical stratification is greater during the entire tidal cycle (Fig. 9h). Vertical stratification is greatest during late ebb and smallest during late flood, which is typical for the classical tidal straining mechanism. This process, therefore, mainly modifies the vertical current structure in one-dimensional, along-stream, direction (Fig. 9e). These simulations only explain the mid-depth velocity maximum during the early flood phase, because the peak flood currents in the Marsdiep are generally able to mix the entire water column during peak flood. It is therefore implausible that vertical stratification during late flood is a relic from classical tidal straining generated during ebb.

Only the presence of a weakly-stratified water column is required to generate a mid-depth velocity maximum under such a high current regime. The transition from well-mixed to weakly-stratified conditions from peak to slack currents is exemplified in the left and middle column of Fig. 9 and shows that the great water depth enables this shift. The right column of Fig. 9 shows that smaller water depths experience well-mixed conditions under a smaller tidal forcing (run 3). A greater water depth creates a greater variation in vertical stratification over the tidal cycle (Fig. 9h and i).

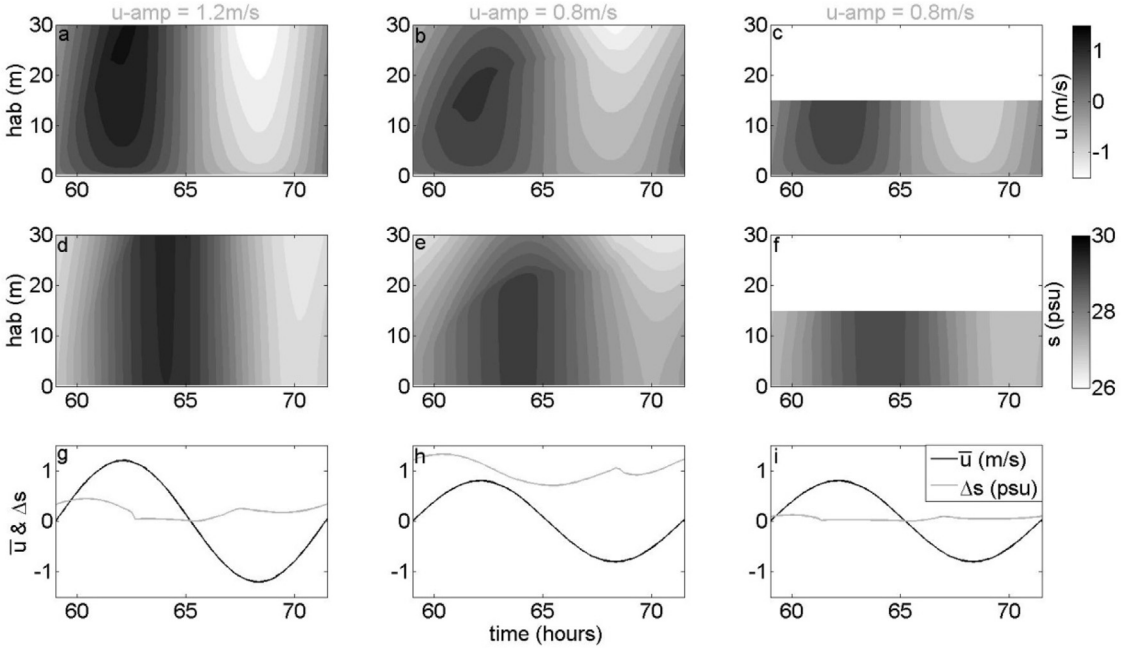

Fig. 9. Model output of current velocities (upper row) and salinity (middle row) during 1 tidal cycle of the idealized model scenarios (runs 1–3). The *x*- and *y*-axes represent time and height above the bed, respectively. In the lower row, the depth-averaged current velocity ($\bar{u}$, black line) and the top-to-bottom salinity difference (Δs, gray line) are depicted as a function of time. The left, middle and right columns represent model runs with tidal amplitudes of 1.2, 0.8 and 0.8 m/s, respectively.

The stratifying dynamics are further investigated using the Simpson number. The Simpson number, *Si*, which was previously called the horizontal Richardson number, (e.g. Stacey et al., 2008, 2010), displays the (one-dimensional) balance between the stratifying and de-stratifying forces in the water column as a function of the horizontal salinity gradient, d*s*/d*x* (psu/m), water depth, *H* (m), and the friction velocity, u_* (m/s), where the latter represents the kinetic energy of the currents:

$$Si = \frac{g\beta(\partial s/\partial x)H^2}{u_*^2}, \tag{10}$$

where g is the gravitational acceleration (9.81 m/s^2) and β is the haline contraction coefficient (7.7×10^{-4}). A *Si* value greater than 1 indicates that the potential energy is greater than the kinetic energy which implies that the water column remains vertically-stratified during the entire tidal cycle. Stacey and Ralston (2005) and Burchard et al. (2011) demonstrated that tidal straining is important for $Si > 0.2$. A small friction velocity of 0.05 m/s, approximately 1/3max(u_*), and a tidally-averaged d*s*/d*x* of 2×10^{-4} psu/m in a water depth of 30 m are representative values for the Marsdiep (De Vries et al., 2014), and results in a *Si* of 0.54, sufficient to allow vertical stratification by tidal straining during weak currents. Peak currents are characterized by Si values of approximately 0.05 and imply well-mixed conditions.

To evaluate under which Simpson numbers along-stream tidal straining generates a mid-depth velocity maximum during the entire flood tide, the height of the mid-depth velocity maximum during peak flood is assessed for a range of Simpson numbers. A total of 39 model simulations are run with varying tidal amplitudes (and therefore varying friction velocities), which produce a range of Simpson numbers. The values of *H* (30 m) and d*s*/d*x* (-2×10^{-4} psu/m) are kept constant. The height of the mid-depth velocity maximum is value, normadefined as the height above the bed where the along-stream velocity reaches its maximum lized by the water depth (Z_{MDVM}/H). Fig. 10 shows that *Si* values smaller than 0.35 are characterized by a near-surface velocity maximum. An increase in *Si* between 0.35 and 1 results in the generation and rapid lowering of a mid-depth velocity maximum due to along-stream tidal straining. For high *Si* values, the non-dimensional height of the mid-depth velocity maximum stabilizes to 0.35. Fig. 10 shows that for *Si* values smaller than 0.35, other processes than along-stream tidal straining are responsible for the generation of a mid-depth velocity maximum during peak and late flood, which is discussed in more detail in Section 4.2.

A comparison between the observations and model simulations highlight two main discrepancies. First, along-stream tidal straining only explains the vertical structure of salinity and velocity satisfactorily during early flood since the peak flood currents mix the entire water column. Furthermore, the interaction of the barotropic and baroclinic pressure gradients in GOTM results in the greatest near-bed velocities during flood, which creates the classical estuarine circulation pattern. However, observed near-bed velocities are stronger during ebb than during flood (Fig. 5). This variation in near-bed currents may change the dynamics of vertical stratification and modify the vertical current structure. Semi-realistic scenarios are run to investigate the effect of the observed near-bed velocities on the vertical structure. In addition, the contribution of cross-stream advection of salinity on the generation of vertical stratification during late flood is investigated.

4.2. Semi-realistic scenarios

The asymmetry in near-bed velocities was incorporated using the observed near-bottom along-stream velocities (2 m above the bottom) of *Spring* as a model forcing for neap and spring tide conditions (runs 4–7, Table 2). Neap and spring tide conditions are simulated with a uniform salinity of 28 psu over the entire water column. Alternatively, the effect of vertical stratification generated by non-along-stream processes is incorporated by imposing a two-layer vertical stratification. In Fig. 11, the scenarios are depicted for neap and spring tide conditions with and without a two-layer vertical stratification.

Neap tide conditions are characterized by a mid-depth velocity maximum during the entire flood phase, driven merely by the along-stream advection of salinity (run 4, Fig. 11a and e). The small two-layer vertical stratification increases the strength of the mid-depth velocity maximum (run 5, Fig. 11a, b, e, and f). Fig. 11i and j shows that the vertical stratification is strongest during slack before flood, around 131 h, as a result of tidal straining. However, around 140 h, the second slack before flood, a considerable decrease in vertical stratification is observed as a consequence of the high near-bed velocities during the late ebb phase. The greater near-bed velocities during ebb counteract tidal straining and decrease the vertical stratification during the late ebb phase.

Spring tide conditions without a two-layer vertical

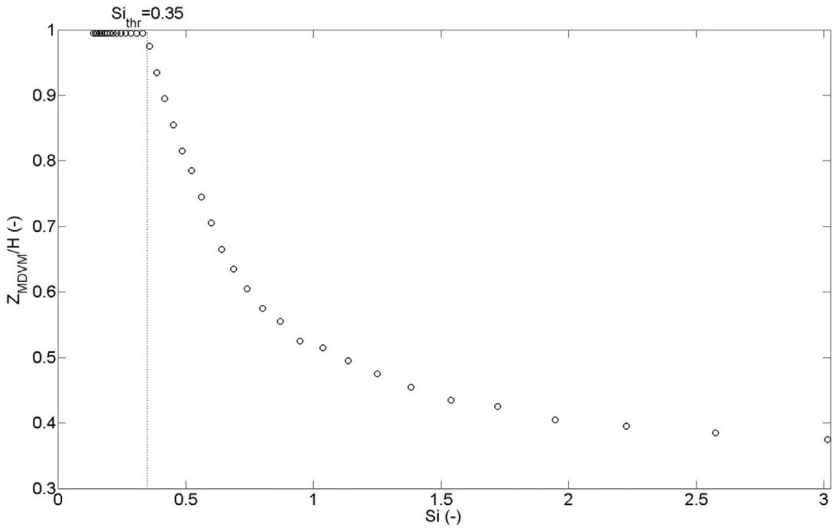

Fig. 10. Relationship between the dimensionless height of the mid-depth velocity maximum (Z_{MDVM}) and the Simpson number based on 39 model simulations where the tidal amplitude is varied.

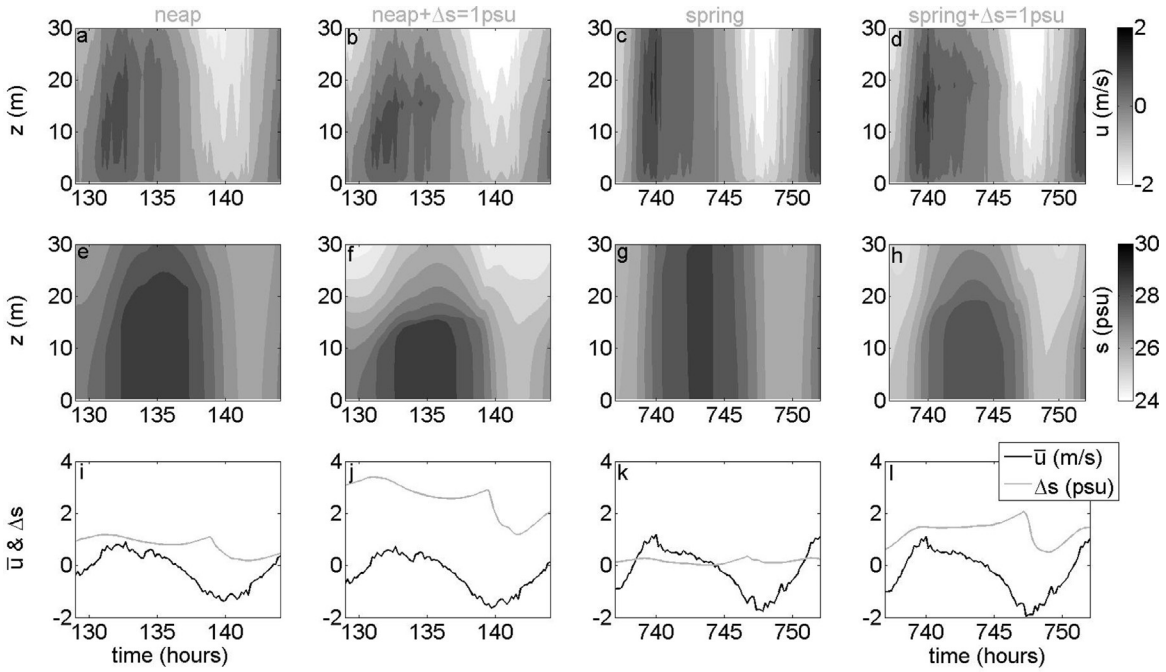

Fig. 11. Same as Fig. 9, but then for the semi-realistic model runs 4–7 in Table 2. Neaptide conditions are given in the first two columns (runs 4 and 5), where in the scenario of the 2nd column a vertical stratification of 1 psu is imposed on the water column. The 3rd and 4th column are organized similarly but then for spring tide conditions (runs 6 and 7).

stratification are characterized by a well-mixed water column during the complete tidal cycle (run 6, Fig. 11c, g, and k). It implies that vertical stratification during spring tide is not only generated by along-stream processes for an along-stream salinity gradient of 2×10^{-4} psu/m. Surprisingly, the superposition of vertical stratification results in the strongest vertical stratification during late flood, in combination with the occurrence of a mid-depth velocity maximum (run 7, Fig. 11d, h, and l). During ebb, the vertical stratification is destroyed (Fig. 11l). The stronger ebb currents and the elevated vertical mixing rates both appear to contribute to the destruction of vertical stratification during ebb. This mechanism, and its effect on the vertical current structure, is most pronounced during spring tide conditions. To investigate if cross-stream processes are able to generate vertical stratification during late flood, as already hypothesized by Van Haren (2010) and De Vries et al. (2014), simulations 8 and 9 were run.

The velocity field of *Spring* in along-stream and cross-stream direction over the entire water column is used to force a neap and spring tide scenario with a constant salinity gradient of 2×10^{-4} psu/m in along-stream and cross-stream (x and y, respectively) directions. Fig. 12 demonstrates that the addition of a cross-stream component has a minor impact on the vertical

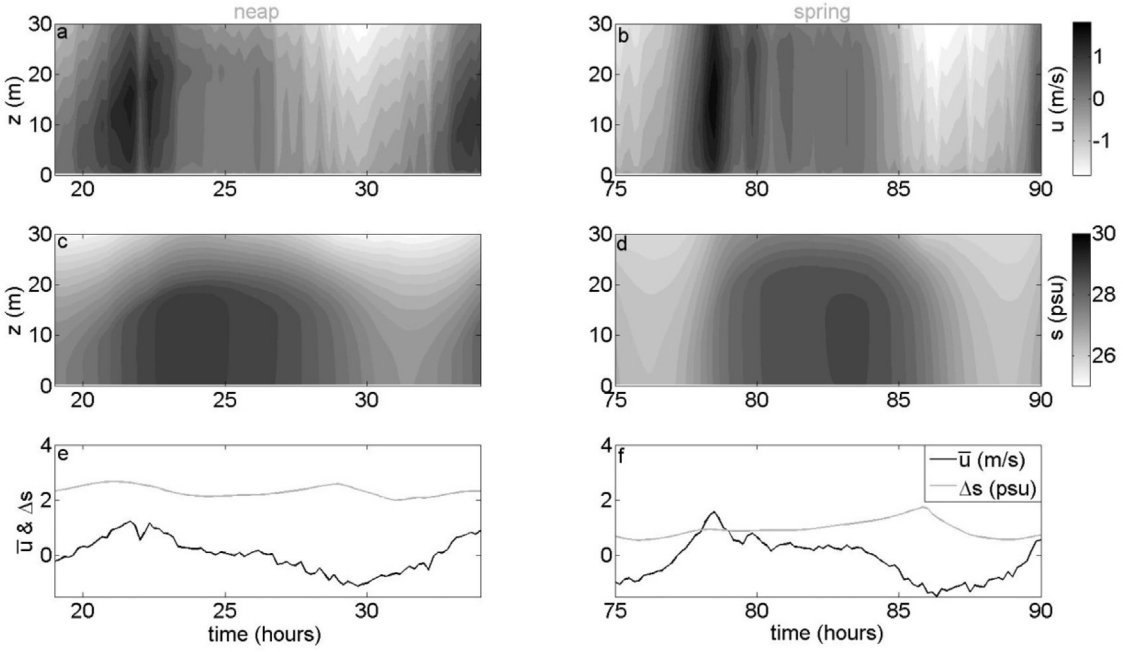

Fig. 12. Same as Fig. 9, but then for semi-realistic model runs 8 and 9 in Table 2. Model output of current velocities and salinity are given for 1 tidal cycle during neap- and springtide (left and right column, respectively). This simulation incorporates advection of salinity by cross-stream currents.

current structure during neap tide (run 8). However, it results in an increase of vertical stratification during the late flood of spring tide (run 9, Fig. 12e and f). Apparently, the rate of salinity advection by cross-stream processes from neap to spring tide increases more strongly than the rate of vertical mixing, which results in an increase of vertical stratification from neap to spring tide conditions. It also explains the presence of a mid-depth velocity maximum during the late flood phase by cross-stream advection of salinity. It suggests a spring neap tidal modulation, and asymmetry, in vertical stratification during late ebb and late flood.

Concluding, the asymmetry in drag coefficient and near-bed velocities results in the destruction of vertical stratification during ebb, which counteracts the tidal straining mechanism. Cross-stream advection of salinity is important during the late flood phase, which creates vertical stratification and generates a mid-depth velocity maximum. In our model runs, both processes appear to increase in importance from neap to spring tide.

5. Discussion

5.1. Near-bed dynamics

Generally, the drag coefficient is assumed constant in the depth-averaged along-channel momentum balance. A constant drag coefficient or a constant eddy viscosity both represent constant vertical mixing rates, which enables a simplification of estuarine dynamics in order to compute the residual circulation by the solution proposed by Pritchard (1956) and Hansen and Rattray (1966). However, several studies have observed asymmetries in the drag coefficient (and eddy viscosity), invalidating the assumption of a constant C_D under certain conditions.

Geyer et al. (2000) observed a constant bed roughness during most of the tidal cycle in the Hudson, an estuary characterized by a uniform bathymetry. However, their observations displayed small but persistent differences between neap and spring tide, also observed in the James River estuary by Li et al. (2004). Seim et al. (2002) observed variations in drag coefficients between 1.5×10^{-3} and 2.5×10^{-3} on the ebb phase depending on the presence of vertical stratification generated by cross-stream currents. Fugate and Chant (2005) observed variations in bed roughness between ebb and flood related to variations in vertical stratification. Fong et al. (2009) observed large variations in C_D not driven by asymmetries in cross-stream currents or vertical stratification but driven by asymmetric bedforms. The drag coefficient was found to be notably greater during flood than during ebb. All these studies relate differences in C_D to 1-D processes in the bottom boundary layer. In addition, at several locations on the continental shelf and in Puget Sound, studies have shown that form drag can contribute substantially to the magnitude of the drag coefficient (e.g. Edwards et al., 2004; Warner et al., 2013).

With the available data, it is impossible to isolate the different contributors to form drag. Empirically, many different parameterizations for bed roughness have been formulated, e.g. the Chézy and Manning coefficient, which incorporate pressure and frictional differences in the drag coefficient by inclusion of the slope of the seabed and/or a roughness length (van Rijn, 2011). It is outside the scope of this research to investigate the factors that contribute to the magnitude of the drag coefficient. However, this study shows that the assumption of a constant drag coefficient is not valid in the Marsdiep basin and that the values are greater than the canonical value of 2.5×10^{-3}. The latter implies that other processes, i.e. vertical stratification, cross-stream advection of momentum and/or form drag influence the near-bed vertical shears. The persistent asymmetry under a wide range of conditions suggests that form drag is the dominant process.

It remains the question to what degree the different spatial scales (sandwave-scale and channel-scale water depth variations) contribute to the drag. The seabed is sloping at the study site, which results in a decrease (increase) in water depth in downstream direction during ebb (flood) and creates a force opposing the ebb current. Furthermore, there is an upstream obstruction during ebb located approximately 1 km up-estuary, which is characterized by water depths 10–15 m smaller than at the study site (Fig. 1b). This might be a source of form drag and could produce elevated values of C_D during ebb. Both characteristics of the bathymetry correspond with the observed asymmetry in C_D, and potentially explain the elevated values.

This study only treats observations at one location. However, the complicated bathymetry is certainly not atypical for the Marsdiep basin. Fig. 1b shows that the channels in the Marsdiep and Vlie basins are characterized by great variations in water depth. It is therefore hypothesized that the magnitude, and asymmetry, of the drag coefficient is spatially highly variable. This hypothesis is supported by the observations in Buijsman and Ridderinkhof (2007a) who observed different values of the friction velocity and drag coefficient in the shallower middle of the Marsdiep inlet with respect to the values presented in this study.

By modifying the intra-tidal vertical mixing characteristics, the asymmetric drag may have implications for the residual circulation. As a result, the residual circulation may therefore be highly spatially variable in complex bathymetries like the Marsdiep basin. Geyer and MacCready (2013) already propose in their review on the estuarine circulation that the along-stream variability of the estuarine circulation requires more research. Here, we suggest that more knowledge on the spatial variability of the drag coefficient, with particular emphasis on form drag, is important for a better understanding of the spatial variability in estuarine circulation for estuaries with a complex bathymetry. Furthermore, numerical models might benefit from the inclusion of a drag coefficient not only dependent on the grain size diameter, but which also depends on e.g. the spatial derivative of water depth.

5.2. Mid-depth velocity maximum

To the authors' knowledge, the observation of a mid-depth velocity maximum occurring separately during both early and late flood has not been made in previous studies. It is interesting that a mid-depth velocity maximum, characteristic of strongly-stratified estuaries, is important in the periodically, and weakly stratified Marsdiep basin. The simulations have shown that the presence of vertical stratification is a requirement for the development of a mid-depth velocity maximum. In the Marsdiep, the peak current conditions are characterized by well-mixed conditions, whereas the early and late phase of the tide are influenced by density-driven processes. The alternation of these regimes results in different generation mechanisms of the mid-depth velocity maxima.

The model simulations imply that vertical stratification generated by tidal straining is sufficient to facilitate the occurrence of a mid-depth velocity maximum during early flood. Cudaback and Jay (2001) demonstrated that strong bed friction is required to decrease the current velocities close to the bed, which applies to the Marsdiep basin. The well-mixed conditions during peak flood inhibit the late flood mid-depth velocity maximum to originate from the classical tidal straining. The addition of a realistic cross-stream current and a salinity gradient in the model simulations show that cross-stream tidal straining is a likely candidate to explain vertical stratification generated during late flood.

To further substantiate the claim of the relevance of along- and cross-stream straining in the Marsdiep basin, a scaling of the tidal straining terms is obtained from the dynamic potential energy anomaly equation. For a detailed explanation of all the terms is

referred to Burchard and Hofmeister (2008) and De Boer et al. (2008). The along-stream (S_x) and cross-stream (S_y) tidal straining component are scaled by

$$S_x = \frac{g}{H}\int_{-H}^{\eta} \tilde{u}\frac{\partial \rho}{\partial x} z dz, \tag{11}$$

and

$$S_y = \frac{g}{H}\int_{-H}^{\eta} \tilde{v}\frac{\partial \rho}{\partial y} z dz, \tag{12}$$

where $\tilde{u} = u - \bar{u}$ and $\tilde{v} = v - \bar{v}$ denote the vertical deviation from the mean of the along-stream and cross-stream velocities, respectively. The values of velocity are based on the data of the anchor station depicted in Fig. 4. The values of $\partial\rho/\partial x$ and $\partial\rho/\partial y$ are based on the salinity gradients in Table 1. De Vries et al. (2014) observed the tidally-averaged along- and cross-stream salinity gradients to be of the same order of magnitude in the Marsdiep basin for 2 distinct spatial surveys, being between 1 and 3×10^{-4} kg/m^3/m. Therefore, an along- and cross-stream salinity of the same magnitude (2×10^{-4} kg/m^3/m) is used to evaluate the effects of S_x and S_y. This assumption neglects any intra-tidal variation in along- and cross-stream salinity gradients, but serves well to illustrates at which moments of the tidal cycle cross-stream straining is important. It is not possible to estimate the advective and nonlinear terms of tidal straining with the available data. The goal here is to evaluate the potential role of along-stream and cross-stream tidal straining in the stratification dynamics and their relation to the occurrence of a mid-depth velocity maximum. Using model simulations, Burchard and Hofmeister (2008) and De Boer et al. (2008) showed that the tidal straining term is one of the main mechanisms in estuarine and downstream regions of fresh water influence (ROFI), but they stress that there are great spatial differences.

Fig. 13 shows that along- and cross-stream tidal straining contribute during different phases of the tide, depending on the season. In *Summer*, tidal straining was negligible because of the small salinity gradients. However in *Spring*, along-stream tidal straining has a stratifying (mixing) impact on the water column during ebb (flood). Cross-stream tidal straining stratifies the water column during distinct phases of the tide. During late flood and late ebb, cross-stream tidal straining is important. The stratifying influence of tidal straining is opposed by vertical mixing. The observations and model simulations have shown that the water column is well-mixed during ebb because of the strong currents and corresponding mixing. Therefore, tidal straining during ebb is not able to stratify the water column. The weak currents during late flood enable the generation of vertical stratification by cross-stream tidal straining, which is similar to the differential advection described by Nunes and Simpson (1985) and Lacy et al. (2003).

Differential advection during late flood might be accompanied by advective transport of momentum, which might enhance the development of the along-stream mid-depth velocity maximum. Lower momentum water from the sides of the channel is transported upwards and migrates towards the center of the channel. Simultaneously, higher momentum water is transported downwards in the center of the channel and migrates sideways. Several studies have shown that advective processes contribute to the horizontal momentum balance and impact the strength of the estuarine circulation (Lerczak and Geyer, 2004; Cheng and Valle-Levinson, 2009; Scully et al., 2009a; Burchard et al., 2011; Basdurak et al., 2013). It is complicated to isolate the effects of cross-stream tidal straining and lateral advection of momentum, since they are both related to the strength of the density gradients. So, advection of salinity, and possibly momentum, might both contribute to the development of a mid-depth along-stream velocity maximum, and are both dependent on the density gradients. This study has shown that the presence of weak vertical stratification by cross-stream tidal straining is already sufficient to create a mid-depth along-stream velocity maximum.

Stacey et al. (2008) found, based on idealized model simulations, that the timing of periodic vertical stratification is important for the development of the vertical shears in velocity and for the strength of the estuarine circulation. Stratification imposed on the early flood or early ebb phase produces enhanced shears, which disappear quickly during the high current velocities, whereas vertical stratification imposed during late ebb or late flood has a longer lasting impact on the vertical shears. The shears can remain enhanced until after the succeeding slack tide. The generation of

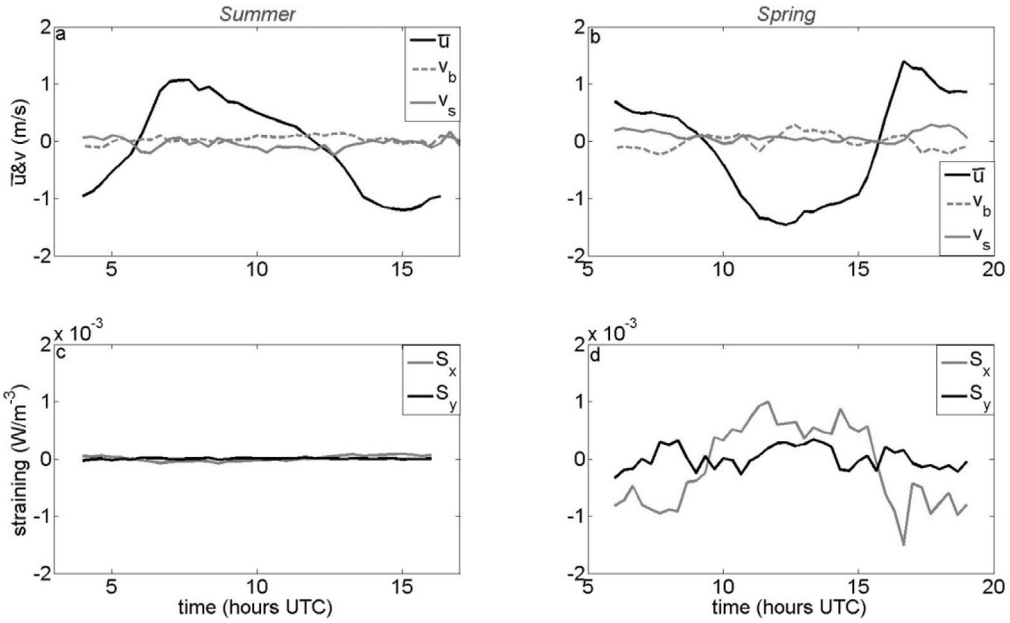

Fig. 13. Along- and cross-stream tidal straining terms during the anchor stations measurements in *Summer* and *Spring* (left and right column, respectively). The upper row displays the depth-averaged along-stream current, $\bar{u}$, and the surface (v_s) and bottom (v_b) cross-stream currents. The lower row displays the along-stream, S_x, and cross-stream, S_y, tidal straining terms as given in Eqs. (11) and (12). The vertical dotted lines indicate the moment of the slack tides.

vertical stratification by cross-stream straining in the Marsdiep basin during late flood suggests that lateral processes can have a great effect on the vertical shears and possibly the strength of the estuarine circulation. However, the enhanced vertical shears simulated by Stacey et al. (2008) contradict with the reversal in sign of the vertical shears in the upper part of the water column as presented in this study, most likely because Stacey et al. (2008) focused on the timing of vertical stratification and neglected the directional effect of the baroclinic pressure gradient.

The variable current dynamics discussed in this study illustrate the importance of two crucial components of the estuarine Marsdiep system. First, the presence or absence of vertical stratification plays an important role in modifying the vertical structure of along-stream velocity. Second, the strong bed friction, probably determined by the complex bathymetry of the sandy seabed, dissipates the tidal energy near the bed and is characterized by an unexpected asymmetry in ebb and flood drag coefficients.

5.3. Spatial and residual current implications

The horizontal circulation cell and corresponding ebb-flood asymmetry in current strength, as described by Buijsman and Ridderinkhof (2007a), might have implications for the shape of the vertical current structure. The northern part of the inlet is characterized by the strongest ebb currents which might therefore be most effective at destroying vertical stratification during late ebb, and thereby counteracting the effect of tidal straining. In the southern part of the inlet, tidal straining might be more important. Furthermore, the observations in this study suggest that the horizontal residual circulation pattern displays a clear spring neap tidal modulation.

The mid-depth velocity maximum during late flood initiates an earlier reversal of the flood current near the surface. This mechanism could increase the estuarine circulation. Several modeling studies have shown that lateral processes are capable of modifying the residual circulation patterns (Lerczak and Geyer, 2004; Scully et al., 2009b; Burchard and Schuttelaars, 2012), which has recently been supported by observations evidence (Basdurak and Valle-Levinson, 2012, 2013). Interestingly, tidal asymmetries and the mid-depth velocity maximum phenomenon are not linearly related to each other since the first is mainly governed by along-stream (one-dimensional) dynamics and the second by along-stream and cross-stream (two-dimensional) processes. Because of these processes, the variability of the residual circulation in the Marsdiep basin deserves further investigation.

6. Conclusions

Hundred days of current and salinity data and simulations with a 1-D water column model were combined to investigate the mechanisms and processes that determine the vertical profile of along-stream velocity in the periodically-stratified Marsdiep basin. The vertical current structure at the study site is characterized by strong bed friction, i.e. a large drag coefficient, which is at least 3–6 times greater than the canonical value of 2.5×10^{-3}. In addition, the friction velocity and near-bed vertical shears are greater during ebb than during flood for the same current magnitude. In estuaries, the superposition of the barotropic and baroclinic tide predicts an opposite asymmetry in friction velocity and near-bed vertical shears. This asymmetry in friction velocity is caused by an asymmetry in bed roughness, which is most likely caused by the complex bathymetry. The simulations show that the asymmetry can result in increased mixing rates during ebb, which can destroy the vertical stratification generated by tidal straining. The importance of this mechanism increases from neap to spring tide.

Higher up in the water column, the vertical shears in along-stream velocity are greater during flood than during ebb. During early and late flood, a mid-depth velocity maximum in along-stream velocity is observed. Both phenomena are generated by different mechanisms. The strong drag coefficient in the area (flood: 7.7×10^{-3}, ebb: 1.25×10^{-2}) and the periodic stratification of the water column are the conditions required to create a mid-depth velocity maximum, as already suggested by Cudaback and Jay (2001) for a strongly-stratified estuary. Vertical stratification during early flood is a relic of tidal straining during late ebb, whereas vertical stratification during late flood is generated by advection of salinity by cross-stream straining. The observations indicate that the strength of the mid-depth velocity maximum is dependent on the strength of the baroclinic pressure gradient.

This study has shown that the baroclinic pressure gradient and the asymmetry in bed friction are both important in shaping the vertical current structure in the Marsdiep basin. The measurements were collected at only one location but similar complex bathymetry in the rest of the Marsdiep basin suggests a more ubiquitous applicability. The mechanisms that enable the destruction and formation of vertical stratification at the study site during ebb and flood, respectively, might have significant effects on the residual circulation.

Acknowledgments

This work is funded by the 'Kansen voor West' KvW-EFRO project 'Ontwikkeling grootschalige inzet offshore getijstroomenergie', No. 21N.010. Three anonymous reviewers and Mark Stacey are thanked for their constructive comments which improved the paper. Last but not least, without the invaluable assistance of the crew of the R.V. Navicula and all the volunteers during the measurements campaigns, this research would not have been possible.

References

Van Aken, H.M., 1986. The onset of seasonal stratification in shelf seas due to differential advection in the presence of a salinity gradient. Cont. Shelf Res. 5 (4), 475–485. http://dx.doi.org/10.1016/0278-4343(86)90071-3.

Aubrey, D.G., Speer, P.E., 1985. A study of non-linear shallow inlet/estuarine Part I: observations. Estuar. Coast. Shelf Sci. 5674, 185–205.

Basdurak, N.B., Valle-Levinson, a, 2013. Tidal variability of lateral advection in a coastal plain estuary. Cont. Shelf Res. 61–62, 85–97. http://dx.doi.org/10.1016/j.csr.2013.04.026.

Basdurak, N.B., Valle-Levinson, A., 2012. Influence of advective accelerations on estuarine exchange at a Chesapeake Bay tributary. J. Phys. Oceanogr. 42 (10), 1617–1634. http://dx.doi.org/10.1175/JPO-D-11-0134.1.

Basdurak, N.B., Valle-Levinson, A., Cheng, P., 2013. Lateral structure of tidal asymmetry in vertical mixing and its impact on exchange flow in a coastal plain estuary. Cont. Shelf Res. 64, 20–32. http://dx.doi.org/10.1016/j.csr.2013.05.005.

Becherer, J., Burchard, H., Flöser, G., Mohrholz, V., Umlauf, L., 2011. Evidence of tidal straining in well-mixed channel flow from micro-structure observations. Geophys. Res. Lett. 38 (17), 2–6. http://dx.doi.org/10.1029/2011GL049005.

De Boer, G.J., Pietrzak, J.D., Winterwerp, J.C., 2008. Using the potential energy anomaly equation to investigate tidal straining and advection of stratification in a region of freshwater influence. Ocean Model. 22 (1–2), 1–11. http://dx.doi.org/10.1016/j.ocemod.2007.12.003.

Buijsman, M.C., Ridderinkhof, H., 2007a. Long-term ferry-ADCP observations of tidal currents in the Marsdiep inlet. J. Sea Res. 57 (4), 237–256. http://dx.doi.org/10.1016/j.seares.2006.11.004.

Buijsman, M.C., Ridderinkhof, H., 2007b. Water transport at subtidal frequencies in the Marsdiep inlet. J. Sea Res. 58 (4), 255–268. http://dx.doi.org/10.1016/j.seares.2007.04.002.

Buijsman, M.C., Ridderinkhof, H., 2008a. Long-term evolution of sand waves in the Marsdiep inlet. I: high-resolution observations. Cont. Shelf Res. 28 (9), 1190–1201. http://dx.doi.org/10.1016/j.csr.2007.10.011.

Buijsman, M.C., Ridderinkhof, H., 2008b. Variability of secondary currents in a weakly stratified tidal inlet with low curvature. Cont. Shelf Res. 28 (14), 1711–1723. http://dx.doi.org/10.1016/j.csr.2008.04.001.

Burchard, H., 1999. Recalculation of surface slopes as forcing for numerical water column models of tidal flow. Appl. Math. Model. 23, 737–755.

Burchard, H., 2009. Combined effects of wind, tide, and horizontal density gradients

on stratification in estuaries and coastal seas. J. Phys. Oceanogr. 39 (9), 2117–2136. http://dx.doi.org/10.1175/2009JPO4142.1.
Burchard, H., Baumert, H., 1995. On the performance of a mixed-layer model based on the k-e turbulence closure. J. Geophys. Res. 100, 8523–8540.
Burchard, H., Bolding, K., 2001. Comparative analysis of four second-moment turbulence closure models for the oceanic mixed layer. J. Phys. Oceanogr. 31 (8), 1943–1968. http://dx.doi.org/10.1175/1520-0485(2001)031 < 1943:CAOFSM > 2.0.CO;2.
Burchard, H., Hetland, R.D., 2010. Quantifying the contributions of tidal straining and gravitational circulation to residual circulation in periodically stratified tidal estuaries. J. Phys. Oceanogr. 40 (6), 1243–1262. http://dx.doi.org/10.1175/2010JPO4270.1.
Burchard, H., Hofmeister, R., 2008. A dynamic equation for the potential energy anomaly for analysing mixing and stratification in estuaries and coastal seas. Estuar. Coast. Shelf Sci. 77, 679–687. http://dx.doi.org/10.1016/j.ecss.2007.10.025.
Burchard, H., Schuttelaars, H.M., 2012. Analysis of tidal straining as driver for estuarine circulation in well-mixed estuaries. J. Phys. Oceanogr. 42 (2), 261–271. http://dx.doi.org/10.1175/JPO-D-11-0110.1.
Burchard, H., Petersen, O., Rippeth, T.P., 1998. Comparing the performance of the Mellor–Yamada the k-e two-equation turbulence models. J. Geophys. Res. 103, 10,543–10,554.
Burchard, H., Hetland, R.D., Schulz, E., Schuttelaars, H.M., 2011. Drivers of residual estuarine circulation in tidally energetic estuaries: straight and irrotational channels with parabolic cross section. J. Phys. Oceanogr. 41 (3), 548–570. http://dx.doi.org/10.1175/2010JPO4453.1.
Canuto, V.M., Howard, A., Cheng, Y., Dubovikov, M.S., 2001. Ocean turbulence. Part I: one-point closure model – momentum and heat vertical diffusivities. J. Phys. Oceanogr. 31, 1413–1426.
Chant, R.J., Geyer, W.R., Houghton, R., Hunter, E., Lerczak, J., 2007. Estuarine boundary layer mixing processes: insights from dye experiments. J. Phys. Oceanogr. 37 (7), 1859–1877. http://dx.doi.org/10.1175/JPO3088.1.
Cheng, P., Valle-Levinson, A., 2009. Influence of lateral advection on residual currents in microtidal estuaries. J. Phys. Oceanogr. 39 (12), 3177–3190. http://dx.doi.org/10.1175/2009JPO4252.1.
Chriss, T.M., Caldwell, D.R., 1982. Evidence for the influence of form drag on bottom boundary layer flow. J. Geophys. Res. 87 (C6), 4148. http://dx.doi.org/10.1029/JC087iC06p04148.
Cudaback, C.N., Jay, D.A., 2001. Tidal asymmetry in an estuarine pycnocline: 2. Transport. J. Geophys. Res. 106 (C2), 2639. http://dx.doi.org/10.1029/2000JC900151.
Dronkers, J., 1986. Tidal asymmetry and estuarine morphology. Neth. J. Sea Res. 20 (2–3), 117–131. http://dx.doi.org/10.1016/0077-7579(86)90036-0.
Duran-Matute, M., Gerkema, T., de Boer, G.J., Nauw, J.J., Gräwe, U., 2014. Residual circulation and freshwater transport in the Dutch Wadden Sea: a numerical modelling study. Ocean Sci. 10 (4), 611–632. http://dx.doi.org/10.5194/os-10-611-2014.
Edwards, K.A., MacCready, P., Moum, J.N., Pawlak, G., Klymak, J.M., Perlin, A., 2004. Form drag and mixing due to tidal flow past a sharp point. J. Phys. Oceanogr. 34, 1297–1312.
Flöser, G., Burchard, H., Riethmüller, R., 2011. Observational evidence for estuarine circulation in the German Wadden Sea. Cont. Shelf Res. 31 (16), 1633–1639. http://dx.doi.org/10.1016/j.csr.2011.03.014.
Fofonoff, N.P., 1985. Physical properties of seawater: a new salinity scale and equation of state for seawater. J. Geophys. Res. 90 (C2), 3332. http://dx.doi.org/10.1029/JC090iC02p03332.
Fong, Da, Monismith, S.G., Stacey, M.T., Burau, J.R., 2009. Turbulent stresses and secondary currents in a tidal-forced channel with significant curvature and asymmetric bed forms. J. Hydraul. Eng. 135 (3), 198–208. http://dx.doi.org/10.1061/(ASCE)0733-9429(2009)135:3(198).
Friedrichs, C.T., Aubrey, D.G., 1988. Non-linear tidal distortion in shallow estuaries : a synthesis. Estuar. Coast. Shelf Sci. 27, 521–545.
Fugate, D.C., Chant, R.J., 2005. Near-bottom shear stresses in a small, highly stratified estuary. J. Geophys. Res. 110 (C3), C03022. http://dx.doi.org/10.1029/2004JC002563.
Geyer, W.R., MacCready, P., 2013. The estuarine circulation. Annu. Rev. Fluid Mech. 46 (1), http://dx.doi.org/10.1146/annurev-fluid-010313-141302 (130829112240001), 175–197.
Geyer, W.R., Trowbridge, J.H., Bowen, M.M., 2000. The dynamics of a partially mixed estuary. J. Phys. Oceanogr. 30, 2035–2048.
Hansen, D.V., Rattray, M., 1966. New dimensions in estuary classification. Limnol. Oceanogr. 11 (3), 319–326.
Van Haren, H., 2010. Very near-bottom tidal straining in a sea strait. Geophys. Res. Lett. 37 (16), 2–6. http://dx.doi.org/10.1029/2010GL044186.
Jay, D.A., Musiak, J.D., 1996. Internal tidal asymmetry in channel flows origins and consequences. Coast. Estuar. Stud. 50, 211–249.
Jay, D.A., Smith, J.D., 1990. Circulation, density distribution and neap-spring transitions in the Columbia River Estuary. Prog. Oceanogr. 25, 81–112.
Lacy, J.R., Monismith, S.G., 2001. Secondary currents in a curved, stratified, estuarine channel. J. Geophys. Res. 106 (2000), 31283–31302.
Lacy, J.R., Stacey, M.T., Burau, J.R., Monismith, S.G., 2003. Interaction of lateral baroclinic forcing and turbulence in an estuary. J. Geophys. Res. 108 (C3), 1–15. http://dx.doi.org/10.1029/2002JC001392.
Lerczak, J.A., Geyer, W.R., 2004. Modeling the lateral circulation in straight, stratified estuaries. J. Phys. Oceanogr. 34, 1410–1428.
Li, C., O'Donnell, J., 1997. Tidally driven residual circulation in shallow estuaries with lateral depth variation. J. Geophys. Res. 102, 27,915–27,929.
Li, C., O'Donnell, J., 2005. The effect of channel length on the residual circulation in tidally dominated channels. J. Phys. Oceanogr. 35, 1826–1840.
Li, C., Valle-Levinson, A., Atkinson, L.P., Wong, K.-C., Lwiza, K.M.M., 2004. Estimation of drag coefficient in James River Estuary using tidal velocity data from a vessel-towed ADCP. J. Geophys. Res. 109 (C3), C03034. http://dx.doi.org/10.1029/2003JC001991.
Li, M., Zhong, L., 2009. Flood–ebb and spring–neap variations of mixing, stratification and circulation in Chesapeake Bay. Cont. Shelf Res. 29 (1), 4–14. http://dx.doi.org/10.1016/j.csr.2007.06.012.
Lueck, R.G., Lu, Y., 1997. The logarithmic layer in a tidal channel. Cont. Shelf Res. 17 (14), 1785–1801.
Maas, L.R.M., van Haren, J.J.M., 1987. Observations on the vertical structure of tidal and inertial currents in the central North Sea. J. Mar. Res. 45 (2), 293–318. http://dx.doi.org/10.1357/002224087788401106.
MacCready, P., Geyer, W.R., 2010. Advances in estuarine physics. Ann. Rev. Mar. Sci. 2 (1), 35–58. http://dx.doi.org/10.1146/annurev-marine-120308-081015.
Moum, J.N., Nash, J.D., 2000. Topographically induced drag and mixing at a small bank on the continental shelf. J. Phys. Oceanogr. 30, 2049–2054.
Murphy, P.L., Valle-Levinson, A., 2008. Tidal and residual circulation in the St. Andrew Bay system, Florida. Cont. Shelf Res. 28 (19), 2678–2688. http://dx.doi.org/10.1016/j.csr.2008.09.003.
Nunes, R.A., Simpson, J.H., 1985. Axial convergence estuary in a well-mixed. Estuar. Coast. Shelf Sci. 20, 637–649.
Pritchard, D.W., 1956. The dynamic structure of a coastal plain estuary. J. Mar. Res. 15, 33–42.
Ridderinkhof, H., 1988. Tidal and residual flows in the Western Dutch Wadden Sea I: numerical model results. Neth. J. Sea Res. 22 (21), 1–21.
Van Rijn, L.C., 2011. Principles of fluid flow and surface waves in rivers, estuaries, seas and oceans. Aqua Publications, Blokzijl, The Netherlands.
Scully, M.E., Friedrichs, C.T., 2007. The importance of tidal and lateral asymmetries in stratification to residual circulation in partially mixed estuaries. J. Phys. Oceanogr. 37 (6), 1496–1511. http://dx.doi.org/10.1175/JPO3071.1.
Scully, M.E., Geyer, W.R., Lerczak, Ja, 2009a. The influence of lateral advection on the residual estuarine circulation: a numerical modeling study of the Hudson River Estuary. J. Phys. Oceanogr. 39 (1), 107–124. http://dx.doi.org/10.1175/2008JPO3952.1.
Scully, M.E., Geyer, W.R., Lerczak, Ja, 2009b. The influence of lateral advection on the residual estuarine circulation: a numerical modeling study of the Hudson River Estuary. J. Phys. Oceanogr. 39 (1), 107–124. http://dx.doi.org/10.1175/2008JPO3952.1.
Seim, H.E., Blanton, J.O., Gross, T., 2002. Direct stress measurements in a shallow, sinuous estuary. Cont. Shelf Res. 22 (11–13), 1565–1578. http://dx.doi.org/10.1016/S0278-4343(02)00029-8.
Simpson, J.H., Brown, J., Matthews, J., Allen, G., 1990. tidal straining, density currents, and stirring in the control of estuarine stratification. Estuaries 13 (2), 125. http://dx.doi.org/10.2307/1351581.
Speer, P.E., Aubrey, D.G., 1985. A study of non-linear shallow inlet/estuarine Part ii : theory tidal propagation systems. Estuar. Coast. Shelf Sci. 21 (5691), 207–224.
Stacey, M.T., 2003. Estimation of diffusive transport of turbulent kinetic energy from acoustic doppler current profiler data. J. Atmos. Ocean. Technol. 20 (6), 927–935.
Stacey, M.T., Ralston, D.K., 2005. The scaling and structure of the estuarine bottom boundary layer. J. Phys. Oceanogr. 35 (1), 55–71. http://dx.doi.org/10.1175/JPO-2672.1.
Stacey, M.T., Burau, J.R., Monismith, S.G., 2001. Creation of residual flows in a partially stratified estuary. J. Geophys. Res. 106, 13–17.
Stacey, M.T., Fram, J.P., Chow, F.K., 2008. Role of tidally periodic density stratification in the creation of estuarine subtidal circulation. J. Geophys. Res. 113 (C8), 1–13. http://dx.doi.org/10.1029/2007JC004581.
Stacey, M.T., Brennan, M.L., Burau, J.R., Monismith, S.G., 2010. The tidally averaged momentum balance in a partially and periodically stratified estuary. J. Phys. Oceanogr. 40 (11), 2418–2434. http://dx.doi.org/10.1175/2010JPO4389.1.
Valle-Levinson, A., 2008. Density-driven exchange flow in terms of the Kelvin and Ekman numbers. J. Geophys. Res. 113 (C4), C04001. http://dx.doi.org/10.1029/2007JC004144.
Valle-levinson, A., Wilson, R.E., 1994. Effects of sill bathymetry, oscillating barotropic forcing and vertical mixing on estuary/ocean exchange. J. Geophys. Res. 99 (93), 5149–5169.
Verspecht, F., Rippeth, T.P., Howarth, M.J., Souza, aJ., Simpson, J.H., Burchard, H., 2009. Processes impacting on stratification in a region of freshwater influence: application to Liverpool Bay. J. Geophys. Res. 114 (C11), C11022. http://dx.doi.org/10.1029/2009JC005475.
De Vries, J.J., van Aken H.M., Nauw J.J., 2012. Variability of currents and vertical stratification in the Marsdiep. In: Proceedings of the NCK-days 2012 Crossing Borders Coastal Research Jubilee Conference, 63, pp. 1–5, 10.3990/2.181.
De Vries, J.J., Nauw, J.J., Ridderinkhof, H., van Aken, H.M., 2014. An exploratory study of the variability of currents and density in the Marsdiep. Cont. Shelf Res. 84, 70–83. http://dx.doi.org/10.1016/j.csr.2014.05.003.
Warner, J.C., 2005. Numerical modeling of an estuary: a comprehensive skill assessment. J. Geophys. Res. 110 (C5), 1–13. http://dx.doi.org/10.1029/2004JC002691.
Warner, S.J., MacCready, P., Moum, J.N., Nash, J.D., 2013. Measurement of tidal form drag using seafloor pressure sensors. J. Phys. Oceanogr. 43 (6), 1150–1172. http://dx.doi.org/10.1175/JPO-D-12-0163.1.
Winant, C.D., Gutierrez de Velosco, G., 2003. Tidal dynamics and residual

circulation in a well-mixed inverse estuary. J. Phys. Oceanogr. 33, 1365–1379.
Zimmerman, J.T.F., 1976a. Mixing and flushing of tidal embayments in the western Dutch Wadden Sea Part I: distribution of salinity and calcutation of mixing time scales. Neth. J. Sea Res. 10 (2), 149–191.
Zimmerman, J.T.F., 1976b. Mixing and flushing of tidal embayments in the Western Dutch Wadden Sea, Part II: analysis of mixing processes. Neth. J. Sea Res. 10 (4), 397–439.
Zimmerman, J.T.F., 1986. The tidal whirlpool: a review of horizontal dispersion by tidal and residual currents. Neth. J. Sea Res. 20 (2–3), 133–154. http://dx.doi.org/10.1016/0077-7579(86)90037-2.